STUDY OF THE PARTICULATE MATTER PRODUCED BY DIESEL AND RENEWABLE DIESEL FUELS ON DIFFERENT COMBUSTION SYSTEMS

**UNIVERSIDAD
DE ANTIOQUIA**

1 8 0 3

UNIVERSIDAD DE ANTIOQUIA
FACULTAD DE INGENIERÍA

PhD THESIS

Presented by

Marlon Cadrazco Ospino

Advisors

Dr. John Ramiro Agudelo Santamaría

Dr. Alexander Santamaría Palacio

March 2019

ABSTRACT

Renewable diesel (RD), a paraffinic fuel produced by the hydrotreating fatty acids, is gaining worldwide interest due to its significant low particulate emissions and its potential in advanced combustion studies. Multiple works reported that RD has good engine performance and emission characteristics, but the literature about soot properties is still limited. This work used three different combustion systems to examine the influence of RD on the particulate matter characteristics. RD was used neat and blended with ultra-low sulfur diesel (ULSD) to generate particles in i) an automotive diesel engine (running at fixed engine torque and two engine speed), ii) a partially premixed flame burner (under a fixed equivalence ratio), and iii) a non-premixed flame burner (wick-fed configuration). The pool of characterization techniques performed in this work comprises thermogravimetric analysis (TGA) for oxidation reactivity and active surface area (ASA); Raman spectroscopy and X-Ray diffraction (XRD) for bulk internal structure; high-resolution transmission electron microscopy (HRTEM) for soot morphology and fringe parameters; Fourier transform infrared spectroscopy (FTIR) for functional groups; and scanning mobility particle sizing (SMPS) for particle size distributions (PSD).

Engine experiments indicated that diesel soot is slightly more reactive to oxidation than the soot produced by RD and its blends, independently of the engine speed. This behavior was in agreement with the active surface area (ASA) of the particles. Soot nanostructure (ratio of Raman peaks) and interlayer distance show a slightly higher degree of order in the particles when RD was added into diesel fuel, which was consistent with their lower reactivity. The mean primary particle diameter of neat RD samples and fractal dimension were lower in comparison with ULSD samples. Fringe analysis applied to HRTEM micrographs revealed no clear trend in the fringe length and tortuosity. In addition, it was found that independently of the fuel tested, all particle samples gathered at 2410 min^{-1} were slightly more reactive and smaller than those collected at 1890 min^{-1}.

The examination of the physical and chemical features of particles generated in flame burners supported the results obtained in the engine study. This is, particles generated by neat RD in both flame environments showed more graphite-like domains than those from ULSD. This result is in line with both an increased intensity of C=C stretch in infrared spectra and smaller interlayer distance. SMPS results showed that RD not only moved the size distribution toward smaller diameters but also

increased the number of ultrafine particles. As expected, a reduction in mass emission was evidenced when the NPF burner was fuelled with neat RD. Raman parameters and the mean primary particle showed interesting relationships when the same fuel was burned in different combustion system.

Highlights

This research pretends to deliver information to the scientific community regarding to this promising paraffinic fuel. Certainly, the acquired knowledge would provide additional tools to the existing ones for improvements in environmental regulations.

The novelty of this research is:

- For the first time, particle characterization is performed on samples produced by partially premixed flames of renewable diesel.
- For the first time, renewable diesel is used to compare the characteristics of engine-derived soot and flame-derived soot.

ACKNOWLEDGEMENTS

DEDICATION

I wish to dedicate this thesis to the five most important and influential people in my life, Daniela, Mabel, Stefanny, Jennifer and Justin. Thank you for your emotional support.

TABLE OF CONTENTS

LIST OF FIGURES

LIST OF TABLES

NOMENCLATURE

ASA	active surface area
CO	carbon monoxide
CO_2	carbon dioxide
d_{002}	interlayer distance
D_f	fractal dimension
DPF	diesel particulate filter
d_{pp}	mean primary particle diameter
EGR	exhaust gas recycle
FAME	fatty acids methyl esters
FT	Fischer-Tropsch
FTIR	Fourier transform infrared spectroscopy
GTL	gas-to-liquid fuel
HRTEM	high resolution transmission electron microscopy
HVO	hydrotreated vegetable oil
L_a	fringe length
L_c	crystallite height
$MLRT_{max}$	maximum mass loss rate temperature
NOx	nitrogen oxides
NPF	non-premixed flame
PAH	polycyclic aromatic hydrocarbons
PM	particulate matter
PPF	partially premixed flame
PSD	particle size distribution
RD	renewable diesel
RD10	volumetric blend of 10% RD and 90% ULSD
RD30	volumetric blend of 30% RD and 70% ULSD
RD	neat renewable diesel
SMPS	scanning mobility particle sizer
T_{exh}	exhaust temperature
TGA	thermogravimetric analysis
THC	total hydrocarbons
ULSD	ultra-low-sulfur diesel
VOF	volatile organic fraction
XRD	X-ray diffraction

Chapter 1
INTRODUCTION

1.1. Problem description

About 20% of the world primary energy is consumed by transportation sector and it is almost entirely provided by fossil fuels (85%) [1]. It is well known that their use in vehicles produce a large amount of contaminants impacting negatively on the environment and health. Particularly, diesel particulate matter (PM) not only alters the air quality in urban centers (visibility impairment and smog), but also increase the risk of acute and chronic respiratory diseases. In fact, PM has been classified by the International Agency for Research on Cancer (IARC) as "carcinogenic to humans" (group 1) since June 2012 [2]. Carcinogenicity of the PM has been related not only to strong genotoxicity of the adsorbed polyaromatic hydrocarbons (PAH) on the particles surface but also to mutagenic effects showed by extracts of PM [3]. As a result, government agencies have introduced stringent regulations regarding to the emission of PM into the environment and scientific community have been proposed several alternatives to match those regulation requirements. Advanced concepts in diesel combustion, new diesel engine technologies, exhaust aftertreatment devices and alternative fuels arise as prominent research solutions to meet the emission legislations.

Before the consolidation of any alternative fuel in the transportation sector, an extensive evaluation including the study of PM characteristics should be conducted. This assessment could be done on i) engine test benches, emulating real operating conditions or ii) through laboratory flames, which are a valuable tool that removes the thermo-fluid interactions occurring inside the engine cylinder (enabling to establish the impact of fuel chemical composition alone). However, both approaches are rarely addressed in conjunction, or limited studies are available in flame burners using commercial fuels. In relation to the study of non-conventional fuels in diesel engines, oxygenated fuels like alcohols and biodiesel (fatty acids methyl esters, FAME) have proven to be successful in PM reduction and have been extensively accepted as partial diesel fuel substitutes [4]. Nevertheless, they have some technical issues (blending limitations, due to fuel stability and changes in diesel properties) and emission concerns (biodiesel increases NOx and alcohols increase unregulated emissions like aldehydes). Renewable diesel fuel (hydrotreated vegetable oil, HVO) is another bio-derived fuel that is gaining worldwide interest because of its good engine performance and low emissions characteristics [5], but the studies reported to date about the characteristics of the generated particles is still scarce.

1.2. Literature review

1.2.1. Renewable diesel

Renewable diesel (from now on referred as RD) is a lipid-derived biofuel that seems to be a promising substitute of conventional diesel fuel for the automotive industry, due to its potential in advanced combustion research [6], allowing the development of new generation engine technologies. RD has some advantages over FAME such as higher biofuel concentration in the blend while meeting the EN590 standard, production costs, storage stability, NOx emissions, tendency to dilute engine oil and adaptability to current engine designs [7, 8]. Moreover, RD has high cetane number (CN > 80), high heating value by mass (~44 MJ/kg), and additionally, it is free of aromatic, oxygen and sulphur compounds [9, 10].

Properties of the RD are quite similar to those of synthetic Fischer-Tropsch (FT) diesel fuels (commonly called XTL fuels), which also have shown significant improvements in all regulated emissions [11]. In fact, due to their paraffinic nature, the quality requirements for RD and XTL fuels are further defined in the DIN EN 15940:2018 standard. RD and low-temperature FT fuel (LTFT, or gas-to-liquid -GTL-) are the most commercially advanced fuels available on the market as fossil diesel fuel substitutes, nevertheless, RD is projected to be produced at one-third of the cost of FT fuels [6].

The common pathway to produce RD is by hydrotreating catalysis of fatty acids at high temperature (300-450 °C) and high pressure hydrogen (50-90 bar), where oxygen atoms are removed from the structure of the triglycerides and the carbon double bonds are saturated to obtain linear paraffins (C_{15}-C_{18}) [12] and by-products as water vapor, carbon dioxide CO_2 and propane [13]. RD production is interesting because it can be integrated into the conventional refinery hydroprocessing facilities, thus lowering capital costs [14].

1.2.2. Studies about renewable diesel in diesel engines

Most of the related research has shown that without modifying any engine parameter, RD (neat or blended with diesel fuel) provides better engine efficiency [15-18] and reduces regulated emissions (CO, THC, NOx and particulate matter -PM-) [6, 8, 14, 19-25], and unregulated pollutants like polycyclic aromatic hydrocarbons (PAH) and aldehydes [26-30] when compared to conventional diesel fuel. Moreover, when engine parameters are optimized for RD, such as injection timing and rates of exhaust gas recycle (EGR), further emission reductions can be achieved (especially for NOx) [20, 31-38]. According to refs. [22, 33], RD reduces the HC and CO emissions due to its high cetane number

(shorter ignition delay) and its low T90 temperature (better fuel evaporation). Also refs. [22, 33, 38] stated that its lower distillation range and the absence of sulfur and aromatic hydrocarbons (soot precursors) cause a decrease in PM emissions. Additionally, the high H/C ratio of RD reduces the flame temperature which results in lower thermal NO production [16, 21] although it seems that there is a strong dependence on engine type and technology [39].

The effect of RD on PM characteristics is a nascent research and few works have been published. Happonen et al. [40] compared the oxidation of soot samples produced with RD and diesel fuel by observing the particle size reduction in a high-temperature tube furnace. They concluded that there were no significant differences between soot oxidation characteristics for the fuels tested. The interlayer distance for RD derived soot was slightly higher than diesel soot, but results were not conclusive. Electron energy loss spectroscopy (EELS) also showed close similarities in the soot surface structure.

Bhardwaj et al. [41, 42] showed that RD derived soot exhibited higher reactivity compared to the soot produced by diesel fuel. They stated that higher soot oxidation rates of RD could be explained by i) the small primary particle size of the RD soot which increases exposure to oxygen due to high specific surface area; ii) the more disordered microstructure of RD determined through HRTEM and XRD; and iii) the low C/O ratio of RD which indicates high oxygen content on soot structure.

Lapuerta et al. [43] found that soot produced by RD and GTL oxidizes at lower temperatures compared to diesel soot due to the concentration of oxygenated hydroxyl group detected by DRIFT. They also stated that additional improvements in soot reactivity could be achieved by calibrating engine operating parameters. Rodríguez-Fernández et al. [44, 45] found that paraffinic fuels (RD and GTL) produced particles with similar oxidation rates between them, but both soots oxidized faster in comparison with diesel particles. They correlated the enhanced reactivity with the high specific surface area of RD and GTL particulate matter (calculated from particle size distributions).

A recent study performed by Sun [46] evaluated the oxidation behavior of PM produced by ULSD, GTL and RD under conventional and partially-premixed charge compression ignition (PCCI) combustion modes. This work demonstrated that PCCI combustion produced soot with significantly higher reactivity compared to conventional combustion. However, in contrast to above studies it was stated that paraffinic fuels produced soot with lower reactivity compared to ULSD. The reaction rate

constants of soot from LTFT and RD fuels were similar but 47-66% lower than soot produced from ULSD. It was argued that the shortened ignition delay (due to high cetane number of the paraffinic fuels) could increase the local equivalence ratio and combustion temperature, yielding a more mature soot (more ordered nanostructure) with lower reactivity. Other works have also shown that the soot emitted by GTL fuel exhibits lower oxidation reactivity than diesel soot. Song et al. [47, 48] compared the oxidation reactivity and nanostructure of the soot obtained from ULSD and GTL. Both DPF regeneration behavior and kinetic parameters from TGA revealed that diesel soot shows faster oxidation than GTL soot. Although they did not observe any impact of initial soot nanostructure on the oxidation reactivity, they observed a strong effect of the initial oxygen groups. They concluded that, due to its lower content of oxygenated functional groups, GTL soot is unable to form reactive sites that boost the devolatilization and oxidation process. The lower oxidation rate of the paraffinic fuel was also observed by Yehliu et al. [49] who used the same fuels as Song and co-workers, but they found no correlation between surface oxygen content (by XPS) and the reactivity of the soot. Instead, XRD and HRTEM analysis showed that higher soot oxidation of the diesel soot was related to its shorter basal plane diameter (fringe length) and higher fringe tortuosity (increasing the accessible carbons on the edge sites). Author believes that the discrepancies shown in the literature examined could be explained by differences in engine technology, engine operating mode, engine parameters (like injection timing or EGR rates), uncertainties of experimental techniques and in-cylinder complex phenomena associated to PM formation processes.

1.2.3. Studies of particulate matter generated in flame burners fuelled with diesel fuels

There are several studies that uses surrogates in flame burners but very little deal with commercial diesel-like fuels. For instance, Daly and Horn [50] compared the structure of toluene soot and its reactivity to ozone with soot produced from diesel and kerosene. Toluene and kerosene particles were produced in a coflow diffusion flame burner, while diesel soot were gathered from a pressurized diffusion flame. Results showed that, although toluene and kerosene samples were generated under the same combustion conditions, they differs in reactivity due to marked differences in both the nature of organic carbon and the structure of elemental carbon. In contrast, they observed that chemical composition before and after reaction was similar for diesel and toluene samples, despite both soot being produced in different burners. Kerosene soot was the least reactive due to its much more ordered structure (higher presence of aromatic species and higher C/H ratio) and diesel soot was the most reactive because of its amorphous structure (higher aliphatic nature and lower C/H ratio).

Merchan-Merchan et al [51] used a wick-fed diffusion flame to study the structure and size of the soot generated by diesel and biodiesel fuels. Particle nanostructure analysis revealed that biodiesel derived soot possess a highly ordered onion-like structure compared to diesel soot, which presented less graphitic structure consisting in concentrically oriented graphene segments with non-crystalized amorphous material. Their results also showed that biodiesel particles were smaller than those produced by diesel, due to higher temperatures of biodiesel flames (higher oxidative environment). In a recent work and using vaporized coflow diffusion flames, Merchan-Merchan et al. [52] confirmed that the diameter of the particles increases as the diesel fraction in the blend increase. Moreover, when the biodiesel fraction in blended fuel was increased, the chain-like structures became more complex, i.e., long-branched aggregates composed of a high number of primary particles with higher degree of networks in contrast to the short-branched agglomerates formed in the diesel flame.

Witkowski et al. [53] studied the soot volume fraction and the morphology of particles sampled in a laminar coflow methane-air diffusion flame seeded with diesel and surrogate fuel. They found very similar soot volume fractions when toluene was blended with n-tetradecane in similar concentration as the aromatic content of diesel (30 %vol.). However, the primary particle size and radius of gyration were both larger for the diesel than for surrogate fuel, indicating a lower surface growth rate for surrogate relative to the real fuel.

Barrientos et al. [54] studied the effect of fuel-bound oxygen in fatty acid esters on soot oxidation behavior. They burned methyl esters, alkanes, biodiesel and diesel in a co-flow laminar diffusion flame burner. Thermogravimetric analysis showed that the oxidation behavior depends on the length of the alkyl chains, i.e., soot generated from methyl esters with longer carbon chains (biodiesel-like fuels) exhibited lower reactivity compared to those samples derived from shorter alkyl chains. This result suggests not only that the impact of fuel-bound oxygen on the reactivity of soot becomes less significant as the carbon chain length increases, but also that the embedded oxygen in the fuel leads to the formation of soot with a structure with greater accessibility to the sites for oxidation. Raman spectroscopy on samples from methyl esters and n-dodecane confirmed that lower structural order improves the soot oxidation (methyl esters > n-dodecane).They also stated that particles generated by conventional diesel revealed higher reactivity than the soot produced by a high-cetane and low aromatic diesel fuel.

1.3. Objectives

According to literature review discussed above, there is still a lack of knowledge about the effect of RD, as a substitute to fossil diesel fuel, on PM characteristics. With the aim of providing new insights into the use of renewable diesel fuels, this work used an automotive diesel engine and two types of flame burners to address the impact of increasing the fuel paraffinic content (by adding RD into ULSD), on the chemical, nanostructural and morphological characteristics of the PM (Figure 1). It is the first time that multiple characterization techniques are applied to particles generated by renewable diesel in different combustion systems: an automotive diesel engine and two types of flame burners. It is expected that the findings discussed here not only increase the knowledge about soot nature but also provide useful information to establish better fuel policies and to broaden the possibilities of renewable sources in the transportation field.
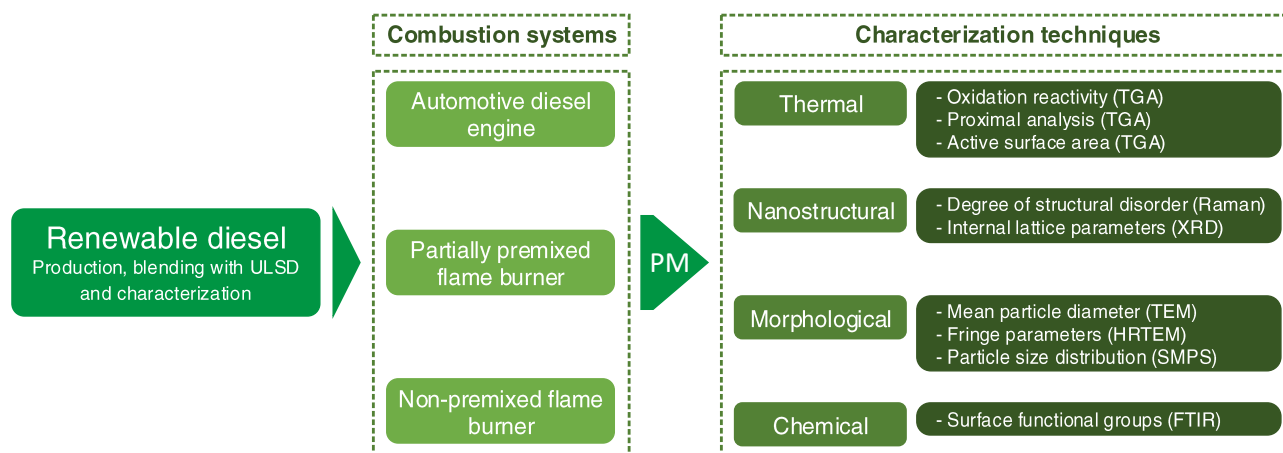
Figure 1.1. Overview of the doctoral thesis.

General objective

To determine the impact of renewable diesel fraction into ULSD on PM thermo-structural characteristics.

Specific objectives

- To establish a relationship between oxidation reactivity and the nanostructural and morphological characteristics of the soot gathered in a diesel engine exhaust.
- To evaluate the characteristics of the soot produced in flame burners.
- To compare the characteristics of soot gathered in diesel engine and flames.

17

1.4. Background of the research groups

The present doctoral thesis was carried out by joining investigation topics of GIMEL (Manejo Eficiente de la Energía) and QUIREMA (Química de Recursos Energéticos y Medio Ambiente) research groups. On the one hand, GIMEL have published multiple works about the characteristics of PM generated in diesel engines fuelled with biofuels like alcohols, biodiesel and vegetable oils. On the other hand, QUIREMA also have reported studies where multiple characterization techniques were applied to soot produced in flames made with hydrocarbons and surrogates with diverse chemical composition. Sampling procedures in both diesel engine exhaust and flames, as well as characterization techniques like TGA, Raman, XRD and FTIR, implemented in previous studies (Figure 1.2) account as background and support most of the methodology employed in the present work. This doctoral thesis not only extends the knowledge about PM nature, but also contributes to the experimental facilities of the involved research groups (construction of flame burner for diesel-like fuels), and provides new methodological tools for soot characterization (e.g. development of application for HRTEM analysis).
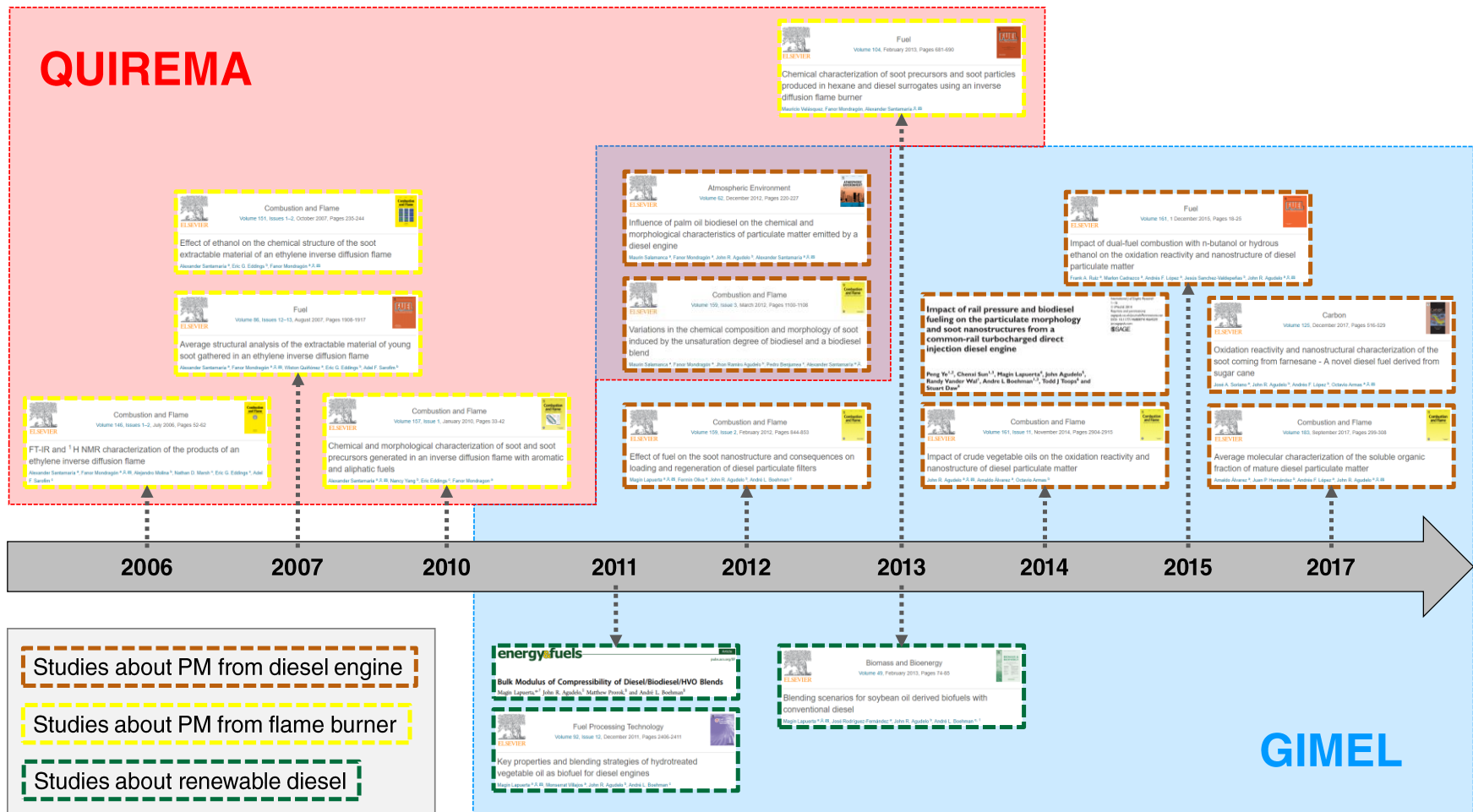
Figure 1.2. Studies conducted in GIMEL and QUIREMA research groups related to renewable diesel and PM characteristics.

Chapter 2
EXPERIMENTAL

2.1. Test fuels

Ultra-low-sulfur diesel (ULSD, supplied by the Colombian petroleum company) was used as a reference fuel for comparison with neat renewable diesel (RD, home produced according to ref. [55]). In short, 2.7 L (2.5 kg) of palm oil was hydrotreated in a 5.5 L Parr high-pressure reactor using 250 g of $(NiMo)S_x/Al_2O_3$ catalyst. The system was heated to 350 °C, pressurized with H_2 at 50 bar and mechanically stirred at 350 rpm during 4 h. Volumetric blend at 10% (RD10) was used as a common blending scenario for biofuels, while RD30 (30%-vol of RD into ULSD) represents a typical blend used in captive fleets which also accounted for around half of the paraffin content in the fuel. Table 2.1 shows the properties of the different fuels tested in this study. The addition of RD into ULSD not only enhances the autoignition quality of the ULSD (increase of cetane number) by increasing its paraffinic fraction, but also reduces the boiling range, the final boiling temperature and the sulfur content.

Table 2.1. Measured properties of the ULSD, RD10, RD30 and neat RD.

Properties	Method	ULSD	RD10	RD30	RD
Density at 15 °C [kg/m^3]	ASTM D4052-11	861	853.95	837.28	780.9
Kinematic viscosity at 40 °C [mm^2/s]	ASTM D445-12	4.356	4.142	3.792	3.086
Lower heating value [MJ/kg]	ASTM D240-09	42.43	42.56	42.82	43.80
Aromatics [% v/v]	-	31.50	28.35	22.05	0
Naphthenes [% v/v]	-	35.95	32.36	25.17	0
Paraffins [% v/v]	-	32.55	39.30	52.78	100
Sulphur content [mg/kg]	ASTM D2622-16	12	< 5	< 5	< 5
C [% w/w]	ASTM D5291-16	86.91	86.72	86.34	84.86
H [% w/w]	ASTM D5291-16	13.09	13.28	13.66	15.14
Mean chemical formula (calculated)	-	$C_{15.06}H_{26.97}$	$C_{15.18}H_{27.64}$	$C_{15.44}H_{29.05}$	$C_{16.53}H_{35.06}$
Boiling range [°C]	ASTM D86-16a	187 - 389	192 - 389	196 - 382	255 - 327
Derived cetane number	ASTM D7668-14	51.36	56.48	67.26	90.94

2.2. Automotive diesel engine

Particulate matter was generated in an automotive diesel engine (Table 2.2.). The engine speed and torque were controlled by a W230 Schenck electromagnetic dynamometer. Engine torque was kept constant at 95 Nm while the engine was run at 2410 min^{-1} and 1890 min^{-1}. At that torque, an engine speed of 2410 min^{-1} leads to maximum smoke opacity according to the Federal Test Procedure (FTP-

75) homologation cycle (which was obtained via vehicle dynamics) [56]. 1890 min^{-1} was selected, among the most representative steady-operation modes. In addition, the exhaust gas recirculation (EGR) was turned off and no any aftertreatment devices were used. Tests were carried out without any modification of the engine parameters or fuel injection system. Before running experiments with a new fuel, the lines were drained, then the fuel was added and the engine operated at least for 30 min in order to purge any fuel remaining from previous experiments.

Table 2.2. Automotive diesel engine characteristics.

Reference	Isuzu 4JA1
Type	4-stroke, direct injection, turbocharged, rotating pump
Configuration	4 in-line cylinders
Swept volumen	2499 cm3
Diameter x stroke	93 mm x 92 mm
Compresion ratio	18.4
Rated power	59kW (80 hp) at 4100 min^{-1}
Maximum torque	98 Nm at 2750 min^{-1}

2.3. Flame burners

In compression ignition engines, fuel atomization and vaporization produce fuel-rich regions that mix with air (coexisting with evaporation) leading to partial premixing [57]. Soot particles are produced in both fuel-rich partially premixed flames and in diffusion flames (formed around droplets of fuel) [58]. Based on that, this study selected these two types of flames in order to emulate the sources of soot generation in typical diesel combustion. For the diffusion (non-premixed) flames, a conventional wick-fed burner was used here, while for the partially premixed flames (PPF), it was adopted the technique reported by Love et al. [59]. They eliminated engine variables like turbulence, injection timing and fuel atomization and vaporization using PPF of prevaporized pure diesel-like fuels. The radiant heat fraction, the emission indices of NOx and CO and the soot volume fraction of both petroleum-derived and biofuels agreed with those obtained from engines studies [59]. Although these authors also provided useful information to understand the dynamics of combustion process of modified fuels, including in-flame profiles of radicals and gas concentration [60], they did not present any information of the impact of fuels on the soot physicochemical features.

A 12-cm length cotton wick with a diameter of 4 mm was housed by a stainless steel fitting placed onto a 50-ml cylindrical glass reservoir (Figure 2.1a) to produced non-premixed flames (NPF). For all fuels, the wick length was adjusted at 5 mm since it was the minimum wick exposure to produce soot in RD fuel. The fuel flow rate, calculated from the weight loss of the burner and measured using a weight

scale, was about 1.27 mg/s for all fuels (see Figure B3 in Appendix B). The flame temperature was measured at different heights of the flame using an R-type thermocouple (Pt 13% Rh/Pt, with wire and bead diameter values of 0.075 and 0.150 mm, respectively) which was placed into the flame by a rapid insertion technique in order to reduce the thermocouple exposure time in sooting flame regions. A Labjack U12 data acquisition system connected to an EI-1040 amplifier were used to record the temperature. Radiation corrections due to heat losses were performed for the thermocouple readings. The uncertainty in all measurements was not larger than 10 °C.

(a)   (b)
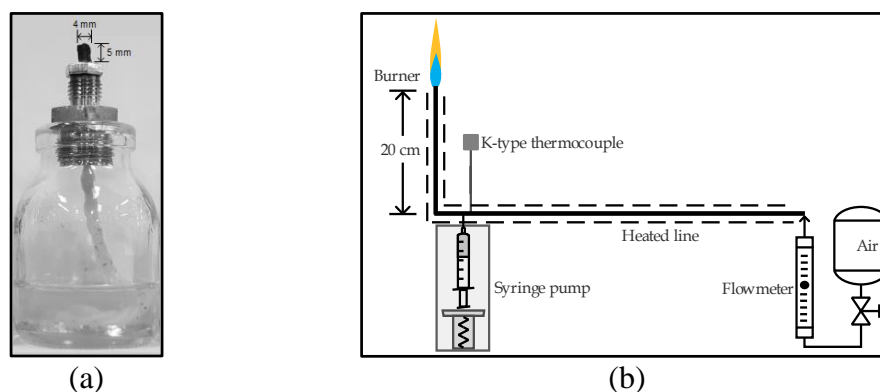
Figure 2.1. Non-premixed flame burner (a) and partially premixed flame burner (b).

Figure 2.1b shows the schematic setup for the partially premixed flames consisting of a 2.1-m stainless steel tube (12.7 OD) wrapped with flexible electric heating tapes used to heat the air up to 400 °C. This temperature was selected because was over the final boiling point of any of the liquid fuels tested (see Table 2.1). A 50-cm^3 syringe actioned by a syringe pump injected the liquid fuel into the high-temperature air stream. The resulting air/fuel vapor mixture flows through a 20-cm stainless steel tube (9.5 mm ID) with a beveled rim. The vertical burner was also heated but at lower temperature (~200 ºC) to avoid fuel auto-ignition. The fuel mixture was ignited at the exit of the burner with an external flame. In order to validate that this burner was able to fully vaporize the fuel, gas chromatography of both raw and vaporized RD was carried out. GC profiles were obtained using an Agilent Technologies 7820A GC with FID detector and a DB-1MS (60 m x 0.25 mm x 0.25 um) column. The two GC spectra (Figure B2 in the Appendix B) showed differences of maximum 4.5% in the intensities of corresponding peaks, indicating that the components in the fuel were completely vaporized. Before performing experiments with a new fuel, an examination of the burner always indicated no presence of coked fuel. Test conditions for this burner are shown in Table 2.3, and were selected after performing a stability map which will be discussed in the results section.

2.4. Sampling procedure and analytical techniques

2.4.1. Sampling procedure

Particulate matter generated in the automotive diesel engine was collected during 1 h of engine operation with a stainless steel mesh filter (Figure C1 in the Appendix C) located 1.5 m downstream from the exhaust manifold, without dilution. The exhaust gas temperature was below 200 °C in order to avoid further PM oxidative reactions. PM was recovered (by shaking softly the mesh) and kept for analysis. This collection method has been used and validated in previous works [43, 61]. Samples generated in the two flame burners were collected at the tip of the flames using glass fiber filters (0.5 μm pore) in line with vacuum system coupled to a 15-cm-length water-cooled stainless steel probe (3 mm ID). The probe has a steel housing that enables support either filters or TEM grids (Figure C2 in the Appendix C). The sampling process was carried out under the same conditions keeping constant the vacuum pressure and time (90 seconds each). In all experiments, the sampling was carried out five times to ensure repeatability.

2.4.2. Thermogravimetric analysis (TGA)

The proximate analysis and oxidation profiles of PM samples were determined with a TA Instruments Q50 thermogravimetric analyzer following the heating programs proposed by Soriano et al. [62] (Table D1 in the Appendix D). The parameter of maximum loss rate temperature ($MLRT_{max}$) [63] and the temperature at which 10% of mass is burned ($T_{10\%}$) were used in this work to compare the thermal behavior of the particulate. The active surface area (ASA) was determined for all PM samples following the procedure described in ref. [64]. A previous repeatability study made with this TG instrument and using diesel soot showed a standard deviation of 1.3 °C for $MLRT_{max}$ (see Figure D1 in Appendix D) and an uncertainty below 6% for ASA tests [62].

2.4.3. Raman spectroscopy

Raman spectra were obtained using a LabRam HR Horiba microscope system equipped with a 632.8 nm He/Ne laser excitation source. For each sample, four different spots were analyzed in a spectral range of 800-2000 cm^{-1} using a magnification objective of 50x. A source power of 0.106 mW and an exposition time of 20 s were used to avoid the burnoff of the sample [65]. Since Raman shifts did not vary significantly when the fuels were changed, the location of the fitting functions were fixed at their average positions [66]: 1160 cm^{-1} (D4, Lorentzian), 1340 cm^{-1} (D1, Lorentzian), 1545 cm^{-1} (D3, Gaussian) and 1605 cm^{-1} (G, Lorentzian). D2 band was not identified on any spectrum. To describe the soot nanostructural features, the area of each curve was compared to the area of G band.

2.4.4. X-Ray diffraction spectroscopy

A Panalytical Xpert Pro MPD diffractometer with copper radiation source ($\lambda = 1.54059$ Å) was used to acquire the XRD spectra of soot samples. The tests were carried out at 45 kV and 40 mA within the range $10 < 2\theta < 60$ with a beam mask of 10 mm, a slit of 0.5 deg., a scan speed of 0.034105 °/s and a step of 0.0263°. The interlayer distance (d_{002}), the stacking thickness of the crystallite (L_c) and their length (L_a) (see Figure 2.3) were obtained by deconvoluting the spectra according to the procedure reported in ref. [61]. The mean value and standard deviation of three spectra were reported here for each soot sample.

2.4.5. High Resolution Transmission Electron Microscopy (HRTEM)

For the samples generated in the diesel engine, the organic fraction of the PM was removed sonically in a dichloromethane bath and the resulting soot samples were dispersed in ethanol. A lacey C/Cu TEM grid were impregnated with drops of the ethanol-soot solution. In the case of flame particles, these were sampled directly on the TEM grid placed in the housing coupled to the probe. The exposure time of the probe was 0.5 s. A FEI Tecnai G2 F20 transmission electron microscope operated at 200 kV was used to obtain images at 38,000x and 43,000x for calculating the mean primary particle diameter (d_{pp}) and fractal analysis. To determine the d_{pp}, particles with distinguishable boundaries were randomly selected and were analyzed by using the image processing software ImageJ®. The fractal dimension (*Df*) of the agglomerates was determined by a home-produced digital image processing software [61], according to the method developed by Lapuerta et al. [67, 68]. To obtain information about the length, tortuosity and separation of the fringes (i.e., interlayer distance d_{002}), the methodology presented in Figure 2.2 was followed. HRTEM images taken at 450,000x and 590,000x of magnification (spatial resolution of 0.024 nm/pixel and 0.019 nm/pixel) were processed using ImageJ® and analyzed with a MATLAB® code (developed following the algorithm proposed by ref. [69]). To facilitate the comparison among fuels, the histograms were converted into curves by connecting the top of the bars with a cubic spline line. Mean primary particle diameter, fractal dimension and fringe analysis were made using 3-6 images per sample.
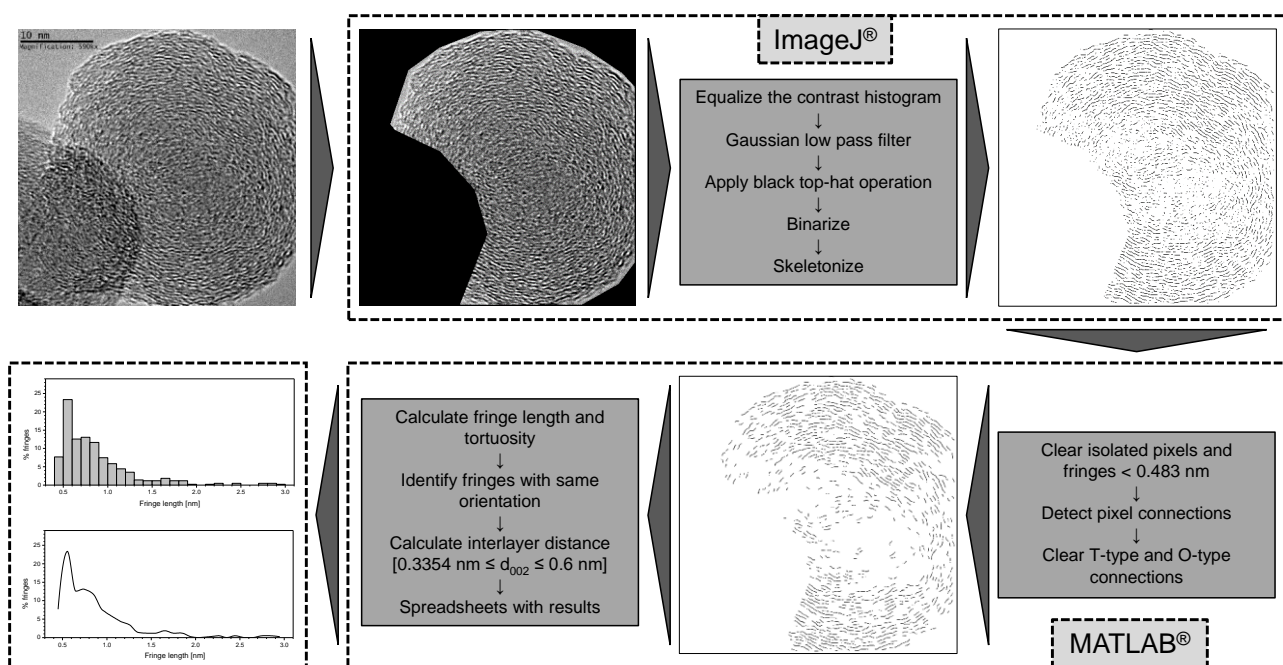
Figure 2.2. Flow chart of the process applied to HRTEM images.

2.4.6. Fourier transform infrared spectroscopy

Functional groups were identified using qualitative Fourier transform infrared spectroscopy (FTIR) analysis. A small amount of raw PM (non-devolatilized) collected was used to prepare a 0.5 wt% KBr pellet. Infrared signals were recorded using a Nicolet 6700 spectrometer with a MCT/A detector. Each spectrum was the result of a 32 scan accumulation, a value that provided the best signal/noise ratio. A blank spectrum was obtained from a KBr pellet prepared without any PM sample to ensure that infrared signals were only attributable to PM chemical compounds and not affected by the preparation process. Three replicates of each sample were taken to estimate repeatability of the method. In general, the uncertainty in the IR measurements was less than 5%. Each spectrum was normalized by the 2920 cm^{-1} intensity as proposed by ref. [70]. This avoided making absolute peak height comparisons among different spectra which can be affected by factors such as the thickness and concentration of the KBr pellet.

2.4.7. X-ray photoelectron spectroscopy (XPS)

A SPECS spectrometer equipped with a Near Ambient Pressure hemispherical Phoibos 150 1D-DLD analyzer was employed to analyze the elemental composition and the carbon-oxygen functional groups on the soot surface. XPS spectra were recorded using a monochromatic Al-Kα (1486.7 eV) X-ray source operated at 10^{-12} bar. The analysis area is roughly 300 μm^2, and the sample surface was oriented normal to the analyzer entrance. For survey scans, samples were scanned 3 times in a range of 0 – 600

25

eV using a pass energy of 90 eV with a step of 1 eV. For high resolution scans C1s (278 – 295 eV) and O1s (527 – 541 eV), samples were scanned 30 times using a pass energy of 20 eV and 0.05 eV step sizes. The soot samples were mounted on double sided conductive carbon tape. The processing of the XPS spectra as well as the estimation of elemental percentages was performed with the CASA XPS software. All the binding energies were calibrated with the C1s binding energy fixed at 284.4 eV as an internal reference. Peak assignments and curve fitting process for C1s and O1s spectra follow the work conducted by Smith et al. [71]. The fitting of all curves was made using a Shirley type background correction and mixed Gaussian and Lorentzian functions (G:L=0.3).

2.4.8. Scanning Mobility Particle Sizer

An Electrostatic Classifier (TSI 3080 with a Kr-85 bipolar charger) coupled to a Nano Differential Mobility Analyzer (TSI 3085) and ultrafine Condensation Particle Counter (TSI 3025 Low Flow) was used to determine the particle size distribution (PSD) of the PM generated in the flame burner. A stainless steel probe (8 mm ID) connected to a #15 Fox Venturi mini-eductor (motive air at 5 psig) was used to pull the particles into the analyzer. With the sheath flow at 3 L/min and the aerosol flow at 0.3 L/min, it was possible to measure particles between 5.14 and 156.8 nm. A scanning time of 2 minutes was used, which corresponds to 4 averaged PSD. Three measurements were registered to obtain the mean and standard deviation values. The PSD includes mathematical correction for particle multiple charges and diffusion losses, both provided by TSI SMPS software. Particle mass distributions were calculated from the PSD and particle density with the methodology proposed by Gomez et al. [72].

2.4.9. Summary of samples characterized

Table 2.4 summarizes the techniques applied to collected samples. As shown, it was not possible to apply every characterization technique to all samples. Due to fuel availability, i) tests with RD were not carried out at 1890 min^{-1} engine speed, and ii) RD10 blend was not prepared for flame experiments, because RD30 blend represents a better intermediate point between ULSD and neat RD. TGA and XRD techniques were not performed to burner-derived particles due to insufficient amount of sample collected in the filters. HRTEM micrographs of the PPF-derived samples were not suitable for fringe analysis due to blurred images (see Figure G1 in the Appendix G) caused by high shakiness of the particles attached to cantilevered agglomerates (composed by numerous primary particles) overhanging from the structures of the lacey carbon grid. PSD were not measured for engine-derived samples because this technique was performed during the doctoral internship at the University of Utah, and the fuel amount required for engine experiments was unavailable. On the other hand, NPF generated PSD

with an incomplete profile, indicating the presence of large particles out of the measurement range of SMPS.

Table 2.3. Samples characterized.

Combustion system	Mode	Fuel	TGA	XRD	XPS	FTIR	Raman	TEM	HRTEM	SMPS
Automotive diesel engine	1890	ULSD	✓	✓		✓	✓	✓	✓	
		RD10	✓	✓		✓	✓	✓	✓	
		RD30	✓	✓		✓	✓	✓	✓	
	2410	ULSD	✓	✓	✓	✓	✓	✓	✓	
		RD10	✓	✓		✓	✓	✓	✓	
		RD30	✓	✓		✓	✓	✓	✓	
		RD	✓	✓	✓	✓	✓	✓	✓	
Partially premixed flame burner		ULSD				✓	✓	✓		✓
		RD30				✓	✓	✓		✓
		RD				✓	✓	✓		✓
Non-premixed flame burner		ULSD				✓	✓	✓	✓	
		RD30				✓	✓	✓	✓	
		RD				✓	✓	✓	✓	

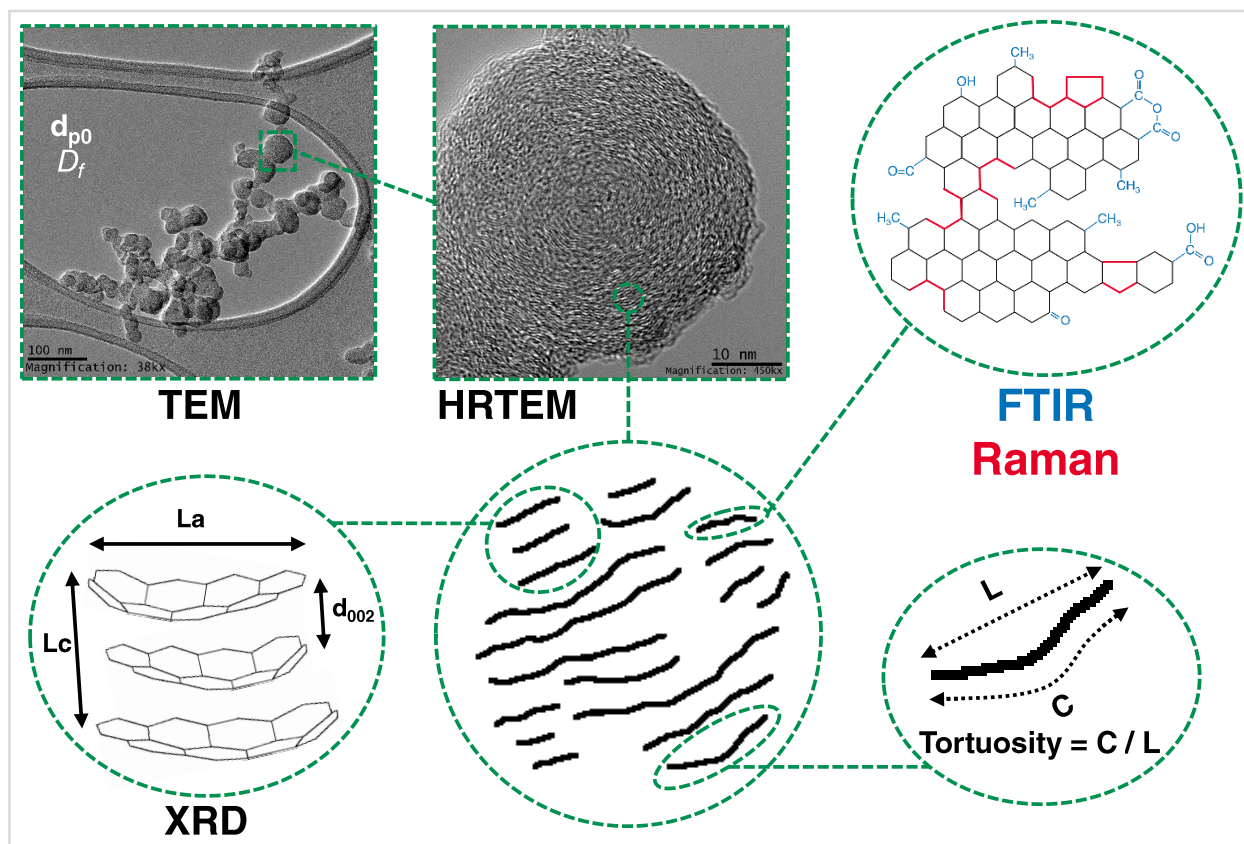
Figure 2.3. Characterization techniques for morphological, nanostructural and chemical analysis.

Chapter 3
RESULTS AND DISCUSSION

3.1. Results related to automotive diesel engine

3.1.1. Oxidation reactivity

Thermogravimetric profiles in Figure 3.1, and data in Table 3.1 show that, although small, the ULSD soot exhibited slightly earlier oxidation compared to RD and their blends independently of engine speed. This result is in agreement with Boehman et al. [47, 49] who reported lower reactivity to oxygen of soot produced by paraffinic fuel (GTL) compared to diesel-derived soot. Barrientos et al. [54], using a co-flow diffusion flame burner, also found that the soot generated by a low aromatic diesel fuel has lower reactivity than a conventional diesel soot. Some works have shown that aromatic compounds in the parent fuel (as is the case of diesel fuel and the blends), improve the oxidation reactivity of the soot [73, 74], maybe because they promote higher disorganized nanostructure in comparison with paraffinic-derived soot [75]. Wei et al. [74] tested in-cylinder soot from the combustion of two diesel surrogates: n-heptane and toluene/n-heptane blend (20% toluene by volume). They found that according to the activation energies obtained by TGA, the soot produced from aromatic-containing fuels was more reactive and also had a more disordered structure (evaluated by EELS and Raman spectroscopy). These findings are also in line with the results presented by Jansma et al. [73], who studied how variations in fuel chemistry (type and amount of aromatics) impact the ease of soot oxidation, as well as, the soot morphology. They demonstrated that soot generated from fuel rich in aromatic compounds (particularly diaromatics) oxidized at lower temperatures than those produced by low-aromatic fuels.

Table 3.1 displays that both $MLRT_{max}$ and $T_{10\%}$ are slightly lower for the soot produced at 2410 min^{-1} indicating early start of reactivity compared to soot generated at 1890 min^{-1}. This agrees with the results of Yehliu et al. [76] who found that higher engine speeds lead to more reactive soot. The oxidation reactivity of diesel particulate matter has been usually explained from the nanostructure and chemical composition standpoints. It has been accepted that more disordered nanostructure [49, 77], as well as the presence of certain aliphatic [78, 79] and oxygenated [47] compounds enhance the soot oxidation. In this work, the oxidation reactivity behavior is explained via the active surface area (ASA) and nanostructure as shown below.
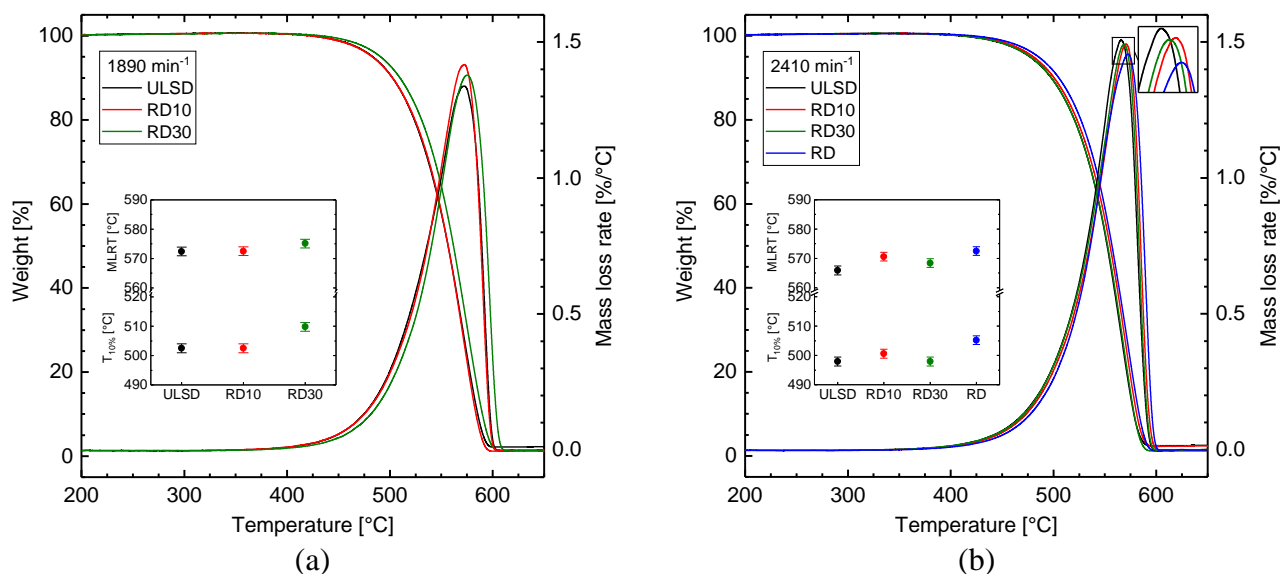
28

Figure 3.1. Thermogravimetric profiles of samples generated at 1890 min^{-1} (a) and 2410 min^{-1} (b).

Table 3.1. Oxidation temperatures, active surface area and proximate analysis.

Speed [min⁻¹]	Fuel	Oxidation temperatures		ASA [m²/g]	Proximate analysis		
		$MLRT_{max}$ [°C]	$T_{10\%}$ [°C]		Ash [%]	Volatile [%]	Carbon [%]
1890	ULSD	572.4	502.5	9.7	2.0	7.9	90.1
	RD10	572.5	502.5	8.1	1.2	8.3	90.6
	RD30	575.1	509.8	7.6	1.2	7.1	91.8
2410	ULSD	565.9	497.9	13.9	2.3	7.9	89.8
	RD10	570.6	500.6	12.5	2.2	8.1	89.7
	RD30	568.4	497.9	12.9	1.1	8.9	90.0
	RD	572.5	505.2	10.8	1.2	7.6	91.3

The overall trend in ASA values (Table 3.1) shows good correlation with $MLRT_{max}$ and $T_{10\%}$ when comparing engine speeds and fuels. It has been accepted in literature that higher soot reactivity is closely related to higher ASA because this in an indication of a high presence of active sites for oxygen reaction [61, 64, 79-81]. it can be seen that diesel soot has higher concentration of ashes compared to RD and their blends. Inorganic ashes in the soot come from the metal compounds in lubricant oil [82]. Lower ash content in RD soot could be associated to the fact that compared to diesel fuel, RD could reduce engine oil dilution due to narrower distillation range and lower final boiling point. It has been observed that metal traces might enhance the soot oxidation rates by increasing the active centers [83, 84], which could also explain the early oxidation behavior of diesel soot compared to RD. In this study, the influence of volatiles on PM oxidation was not taken into account because the oxidation profiles were carried out on devolatilized samples. Regarding the fixed carbon content, it is noted that the

addition of RD to ULSD lead to more carbonized soot independently of engine speed, which is in agreement with the degree of graphitization of the soot shown below.

3.1.2. Soot nanostructure

The Raman spectra of ULSD and neat RD soot samples generated at 2410 min^{-1} were averaged, normalized and depicted in Figure 3.2. Regardless engine speed, it was observed that fuel formulation affects the soot nanostructure. While G band represents ideal graphitic lattices, D1 and D3 bands indicate, respectively, the presence of disordered graphitic structures and amorphous carbon in soot [85]. As the RD concentration increased in the blend, it was observed that the degree of graphitization increased (A_{D1}/A_G decreased, as shown in Figure 3.3). This is consistent with the presence of amorphous carbon (A_{D3}/A_G), which also decreased as RD concentration increased. HRTEM images in Figure 3.2 reveal that although both particles have the typical shell/core nanostructure, ULSD primary particle exhibits a more amorphous center (see red circles) compared to RD soot. Similar result were reported by Wei et al. [74], who showed that n-heptane derived soot had more ordered structure compared to toluene/n-heptane blend soot. Jansma et al. [73] showed that low-aromatic fuels produced particles with more structured morphology than high-aromatic fuels. Vander Wal and Tomasek [77] found that benzene-derived soot has a more amorphous structure than acetylene-derived soot in a premixed flame. No clear trend was observed for A_{D4}/A_G which accounts for double C=C stretch like those of polyene-like structures or ionic impurities [85].
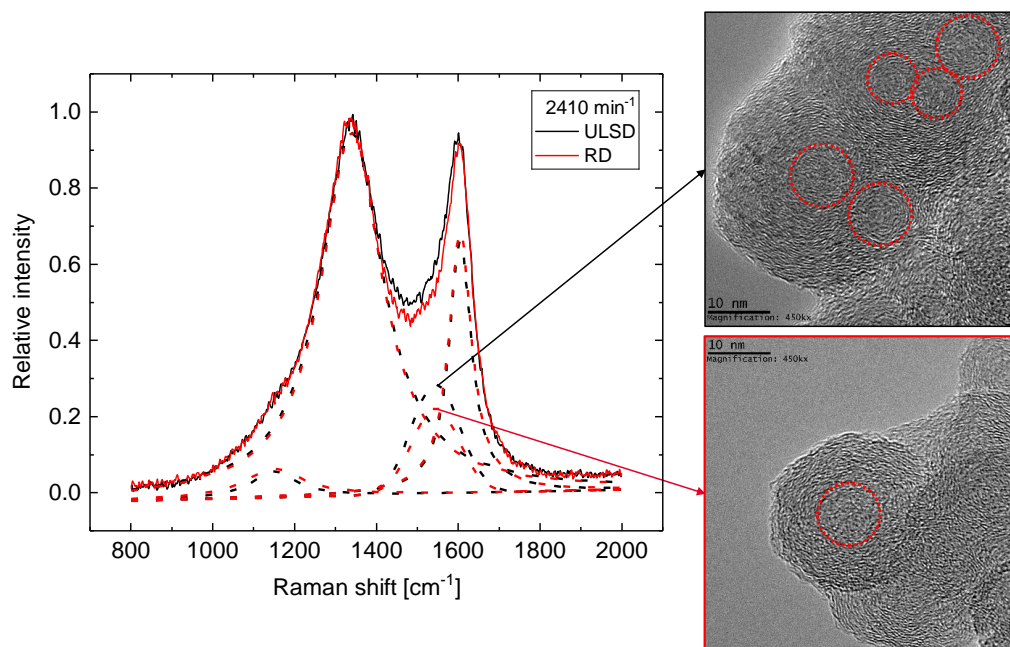

Figure 3.2. Soot nanostructure based on Raman spectroscopy. ULSD and RD spectra.

The differences in nanostructural parameters caused by engine speed are also identified in Figure 3.3 where, in spite of the standard deviations, the mean values showed more ordered soot structure (except for RD30 A_{D3}/A_G ratio) as the engine speed increased. High ordered structure is a consequence of the high-temperature environment in which soot is formed [86]. Table 3.2 provides the exhaust gas temperatures (T_{exh}) for all tests (measured at the exhaust gas turbine inlet). As expected, at constant engine torque, higher engine speeds result in higher temperatures due to power increase. In addition, independently of the engine speed, the combustion of RD and its blends led to higher exhaust gas temperature (T_{exh}), which is a direct indicative of higher in-cylinder gas temperature. Ogunkoya et al. [25] also reported that renewable diesel fuels presented higher exhaust gas temperatures than diesel fuel due to RD high cetane number. When RD is injected in the engine at its default injection timing results in relatively shorter ignition delay, thereby advancing the start of combustion in the cycle, which ultimately raises the pressure and gas temperature in the cylinder [87]. On the other hand, higher combustion temperatures also can be explained by lower soot radiation during RD combustion due to its lower soot emission (as mentioned in literature review). It has been stated that radiation from soot produced in the flame zone is a major source of heat transfer away from the flame, and can lower bulk flame temperatures by 25 K to 125 K, depending on the amount of soot produced at the engine operating conditions [88]. It is observed that T_{exh} values not only follow the overall trend of A_{D1}/A_G and A_{D3}/A_G ratios, but also it is correlated to the fraction of fixed carbon of dry soot (from proximate analysis presented in Table 3.1 above).
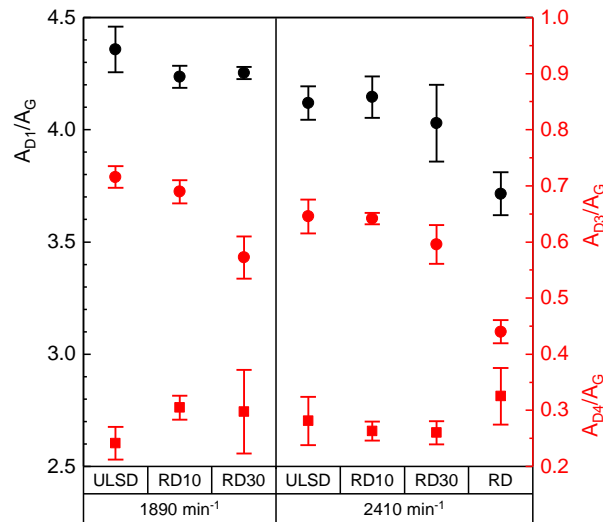

Figure 3.3. Raman peak area ratios.

Lattice parameters obtained by deconvoluting XRD spectra are also presented in Table 3.2. No clear trend was observed for L_c and L_a. However, the mean interlayer distance (d_{002}) is slightly lower for the

soot produced by RD and its blends, independently of the engine speed, evidencing a higher graphite-like nanostructure compared to diesel soot. From Raman and XRD results it can be observed that high soot oxidation reactivity corresponded to high disorder of the carbonaceous nanostructure of the soot, which is in agreement with refs. [49, 64, 74, 77, 89]. A soot with higher graphitization degree has lower available active surface for oxidation [66] and is less susceptible to oxidative attack due to a decreased number of reactive edge site carbon atoms in favor of more stable basal plane sites [90, 91].

Table 3.2. Exhaust temperatures and lattice parameters from XRD analysis.

Speed [min^{-1}]	Fuel	T_{exh} [°C] (SD)	d_{002} [Å] (SD = 0.02)	L_c [Å] (SD = 0.5)	L_a [Å] (SD = 1)
1890	ULSD	464 (4)	3.61	12.1	43.3
	RD10	466 (3)	3.60	12.1	32.1
	RD30	477 (6)	3.59	12.2	34.3
2410	ULSD	473 (6)	3.60	12.2	43.4
	RD10	480 (7)	3.59	12.0	34.2
	RD30	492 (4)	3.57	12.5	36.7
	RD	498 (7)	3.56	12.1	39.1

3.1.3. Soot morphology

Figures 3.4 a-b show two representative TEM images used for determining the mean primary particle diameter (d_{pp}) and fractal dimension (*Df*) of the agglomerates. The box plots show the medians, the means (dots), standard deviations (whiskers), and 25% and 75% percentiles (upper and lower limit of the box). The median shows a slight decrease in the d_{pp} when adding RD into ULSD (Figure 3.5). In agreement with this finding, Sun et al. [6] reported a decrease in the diameter of the primary particles produced by paraffinic fuels (RD and GTL) under conventional combustion. Smaller particle size for RD and its blends could be explained by a high oxidizing environment (see T_{exh} in Table 3.2) that shrinks the primary particles [69]. Song et al. [92] analyzed the effect of sulfur, paraffins, aromatics and naphthene concentrations in the fuel over morphology and nanostructure of particulate samples. Their results suggested that primary particle size increases with sulfur and aromatic content.

2410 min^{-1} engine speed generated smaller sized primary particles compared to 1890 min^{-1}. This result is related not only to high in-cylinder particle oxidation caused by an increase in local temperatures (associated to higher power output at 2410 min^{-1}) but also to the shorter residence time at high engine speed that inhibits the surface growth. Studies conducted with TEM image analysis [93-97] agreed on the fact that increasing engine speed results in a decrease of the size of primary particles, due to shorter residence times for particle surface growth. Furthermore, as evidenced in works carried out with

mobility particle sizers [95, 97, 98] shorter residence times also lower the agglomerate sizes due to reduced number of particle collisions. Table 3.3 displays the mean and standard deviations of fractal analysis. Although no significant differences were found among the soot samples, a decreasing trend in the mean values of *Df* could be noted when RD was used, independently of the engine speed. A lower *Df* implies that RD generated aggregates with an elongated chain-like structure (see Figure 3.4b) in contrast to the aggregates produced by ULSD, which exhibits a more compacted cluster of particles (see Figure 3.4a).
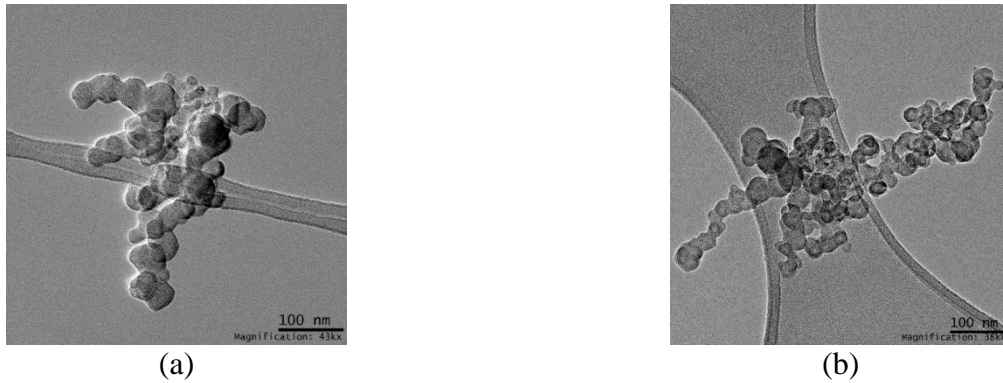

(a)   (b)

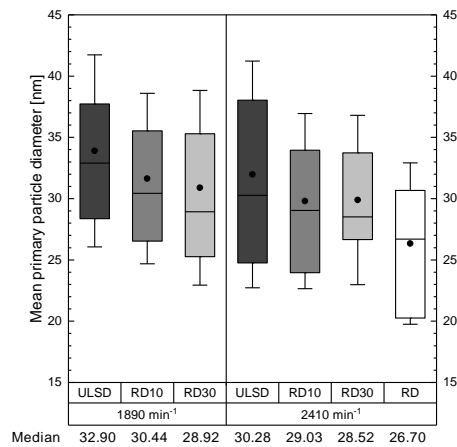Figure 3.4. Representative images of aggregates collected at 2410 min^{-1}: ULSD (a) and RD (b).

Figure 3.5. Mean primary particle
diameter of engine samples.

Table 3.3. Mean primary particle diameter and fractal dimension.

Speed [min⁻¹]	Fuel	d_{pp} (SD)	D_f (SD)
	ULSD	33.90 (7.84)	1.94 (0.29)
1890	RD10	31.64 (6.96)	1.85 (0.37)
	RD30	30.89 (7.94)	1.79 (0.36)
	ULSD	31.99 (9.25)	1.97 (0.30)
2410	RD10	29.80 (7.15)	1.72 (0.21)
	RD30	29.89 (6.92)	1.72 (0.20)
	RD	26.34 (6.58)	1.66 (0.14)

33

The results of the fringe analysis are depicted in Figure 3.6. The box plots show the medians, standard deviations (whiskers), 25% and 75% percentiles (upper and lower limit of the box) and the means (dots) of the three fringe parameters. Although no significant differences were found, both means and medians showed a slight decreasing trend in interlayer distance (d_{002}) with the increasing of RD fraction in ULSD, independently of the engine speed (Figure 3.6 a-b). This means that, compared to ULSD, RD samples have interlayer distance values closer to ideal graphite, indicating more ordered structure, thereby confirming the results of Raman spectroscopy. Although the trend found for d_{002} with HRTEM is consistent with that obtained through XRD analysis, the values are not equal due to differences in the techniques: XRD provides a bulk average interlayer distance, while HRTEM can detect local (but projected) interlayer distances. It has been suggested that shorter d_{002} could hinder the access of oxygen to the edge-site positions, which could result in lower reactivity [99]. No clear trend was encountered for fringe length (Figure 3.6 c-d) and tortuosity (Figure 3.6 e-f). Sun et al. [6] used RD and GTL fuels to compare the soot morphology of particles generated under both conventional and partially premixed compression ignition (PCCI) combustion. Their HRTEM analysis showed that fringe length and tortuosity were not significantly affected by the combustion mode or the type of fuel.
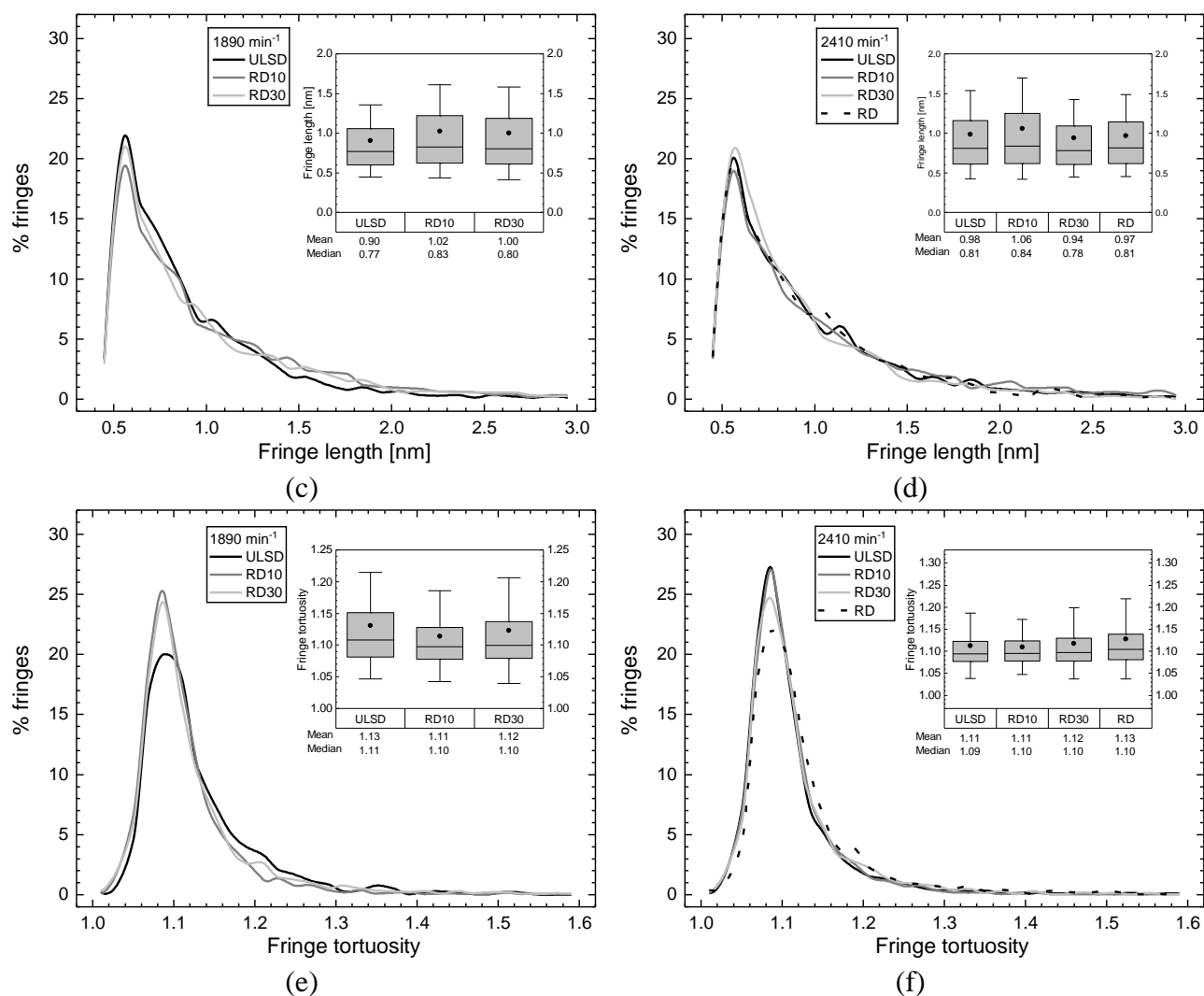

(a)　　　　　　　　　　　　　　　　　　(b)
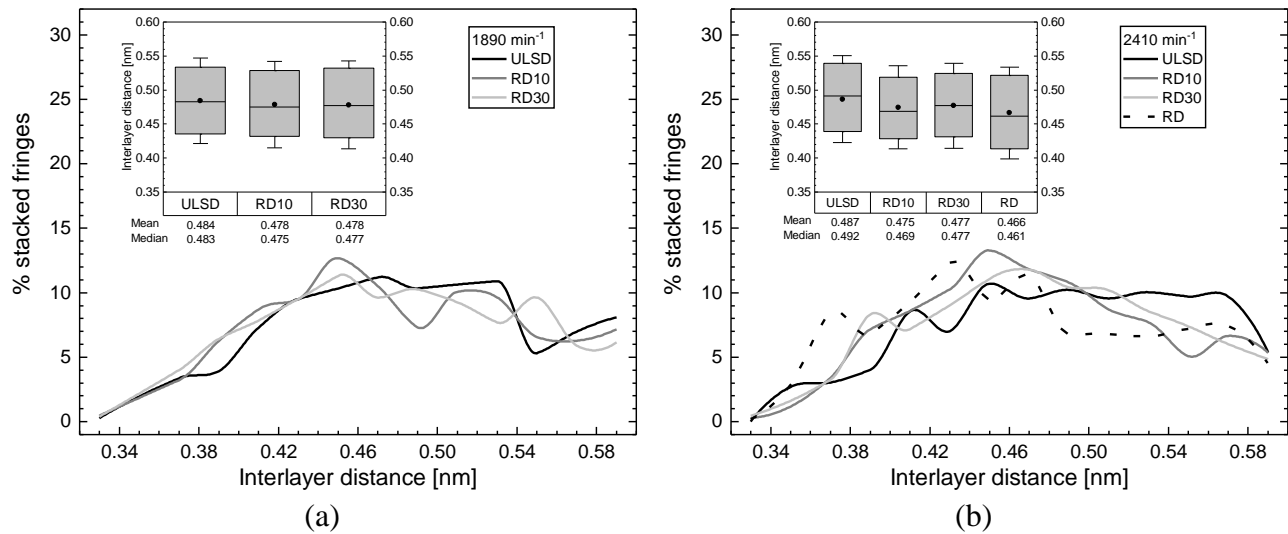
Figure 3.6. Fringe lattice results. Interlayer distance at 1890 min^{-1} (a), 2410 min^{-1} (b). Fringe length at 1890 min^{-1} (c), 2410 min^{-1} (d). Fringe tortuosity at 1890 min^{-1} (e), 2410 min^{-1} (f).

3.1.4. Functional groups

Figure 3.7 displays the infrared spectra of all non-devolatilized PM samples (trends are similar between devolatilized and non-devolatilized samples [70]). Only the fingerprint region (1000 to 1800 cm^{-1}) is plotted due to appreciable variations in the relative intensity of functional groups present in this range. Independent of engine speed, the addition of RD to diesel fuel lead to an increase in the signals of both aliphatic C-H plane deformations of methyl groups (1380 cm^{-1}) and C=C stretching vibrations (1640 cm^{-1}) of olefins and aromatics (Table 3.4). These functionalities could come from both alkyl aromatic hydrocarbons formed due to fuel decomposition and from unburnt fuel that survived the combustion process. In fact, large paraffins decompose during combustion via hydrogen abstraction and/or thermal decomposition to produce smaller alkyl radicals and olefin species through a β scission process [100, 101]. Further, these species can combine each other to form aromatic hydrocarbons including the alkyl

benzene ones which are considered the main building blocks for the soot formation process and growth. The chemical functional groups observed in Figure 3.7 also allows inferring about the temperature-time history experienced by particles in the combustion chamber. The increase in the signal intensity corresponding to the C=C stretching mode (1640 cm^{-1}) put in evidence that the addition of RD produced enough temperature to trigger both the condensation of aromatic systems [102] and particle internal structure organization. This is well correlated with the less disorganized structure revealed by Raman results examined above, and with the XPS analysis shown below. No significant variations were detected in the others functionalities.
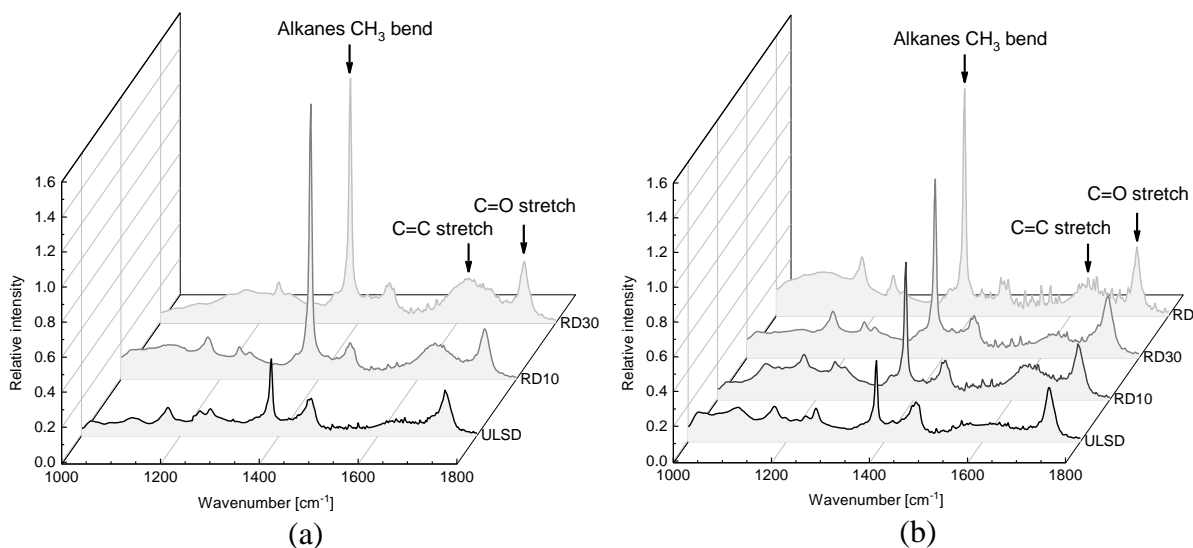

Figure 3.7. FTIR spectroscopy of all soot samples: 1890 min^{-1} (a); 2410 min^{-1} (b).

Table 3.4. Relative intensities of infrared signals of engine samples.

Speed [min^{-1}]	Fuel	Wavenumber [cm^{-1}]	
		1380	1640
1890	ULSD	0.429	0.086
	RD10	1.561	0.198
	RD30	1.386	0.239
2410	ULSD	0.457	0.102
	RD10	0.781	0.195
	RD30	1.018	0.143
	RD	1.297	0.207

Note: Data are normalized to the intensity of the 2920 cm^{-1} signal.

XPS analysis was performed to ULSD and neat RD soot samples as shown in Figure 3.8. C1s and O1s energy regions were deconvoluted into seven and four peaks, respectively, according to the assignments presented in Table 3.5. The surface composition (Figure 3.8a) showed that RD produced

more carbonized soot (96.10 atomic %) than that generated by ULSD (92.97 atomic %). Moreover, compared to ULSD soot, lower surface oxygen content was evidenced in RD soot (7 vs ~4 atomic %).

Table 3.5. Peak assignments for interpretation of C1s and O1s spectra of soot [71]

| Peak	Assignment	Binding energy [eV]	Concentration [%] ULSD	Concentration [%] RD
C-C full	Cyclopentane ring atoms within clusters, fullerene	283.6	3.13	3.53
C-C sp^2	Primary C-C peak, sp2 bonded carbon	284.4	51.35	58.90
C-C sp^3	Cycloheptane or larger rings within clusters, sp3 bonded carbon	285.1	18.12	12.92
C-O	Ether and hydroxyl bonded C, phenols	285.9	7.37	5.08
C=O	Carbonyl groups	286.7	11.37	10.25
COO	Carboxyl, lactone and ester groups	289.2	5.80	5.15
Pi-Pi*	Shake-up satellite peak due to π-π* transitions in aromatic rings	291.0	2.86	4.17
C=**O**	Carbonyl, lactone and carboxyl groups	531.3	27.75	47.10
C-**O** (aliphatics)	Ether and hydroxyl groups bonded to aliphatics	532.5	29.55	1.97
C-**O** (aromatics)	Ether and hydroxyl groups bonded to aromatics	533.3	37.79	40.95
H$_2$O	Absorbed water	535.2	4.91	9.98

Figure 3.8b displays the concentration of the chemical states present in C1s spectra (Figure 3.8c-d) and O1s spectra (Figure 3.8e-f). The sp^2 hybridized carbon (284.4 eV) is considered nearly defect-free graphite, while fullerene (283.6 eV) and sp^3 hybridized carbon (285.1 eV) are defined as defective carbon. RD soot exhibited the highest non-defective carbon content (58.90%), whereas ULSD soot shown the highest defective carbon concentration (21.25%). Moreover, RD samples present a higher concentration of π-π* shake-up satellite peak (291 eV) confirming its higher degree of graphitization [103]. This is in agreement with the results obtained from Raman (Figure 3.3), XRD (d_{002} in Table 3.2), HRTEM (d_{002} in Figures 3.6a-b), and FTIR (Table 3.4) techniques. It has been shown elsewhere [104] that soot with more edge site carbon atoms would be more readily oxidized and can support a higher number of oxygen groups (as is the case of the ULSD soot). Regarding the oxidation state of the carbon (285.9; 286.7, and 289.2 eV) it has been observed that all oxygenated functional groups in the ULSD soot are in larger concentration than in the RD derived soot. This finding is in agreement with the results reported by Vander Wal et al. [91] who found that the highest oxygen content was associated to the soot with the highest sp^3 content. They argued that oxygenated functionalities can only be linked to sp^3 carbon atoms or to carbon atoms located at lamella edge sites. O1s spectra of the two soot samples show a significant change in the aliphatic C-O group (532.5 eV), which shown higher concentration in the surface of ULSD (29.55 at%) and it is strongly reduced in RD soot (1.97 at%). It is hypothesized that the high oxidizing environment in which the RD soot is formed converts the aliphatic groups into C=O groups (531.3 eV, possibly cyclic species like lactones and quinones) and aromatic C-O stretches (533.3 eV). The shifting of the C-O aliphatic peak into C=O and aromatic C-O peaks with the temperature was also observed by Smith et al. [71] using thermoseries of cellulose chars.
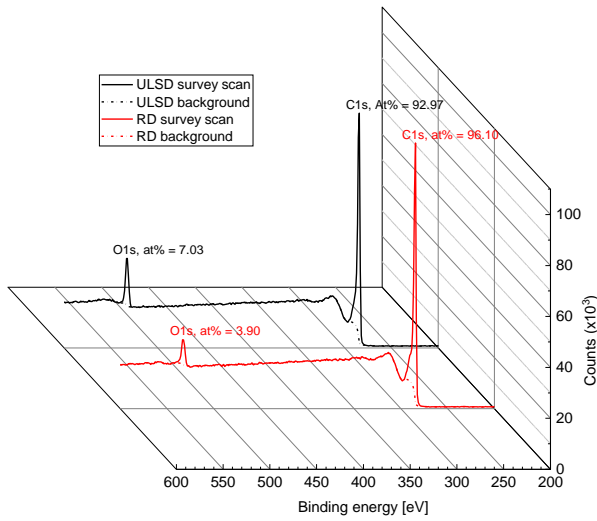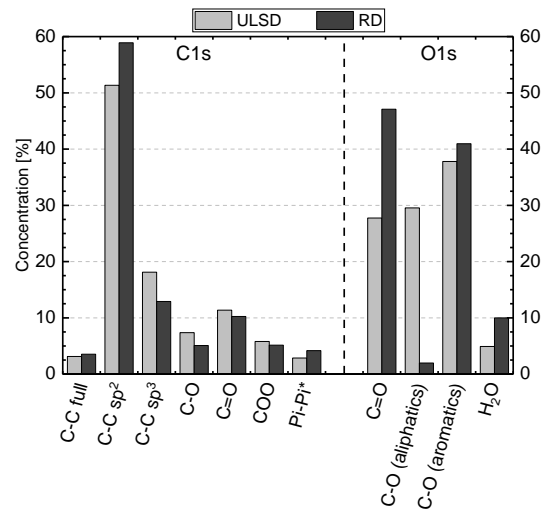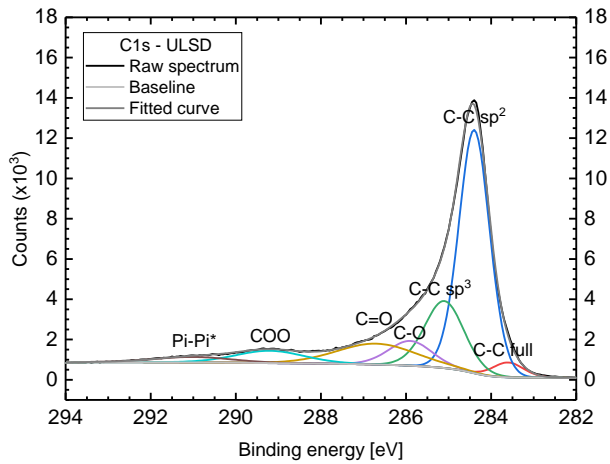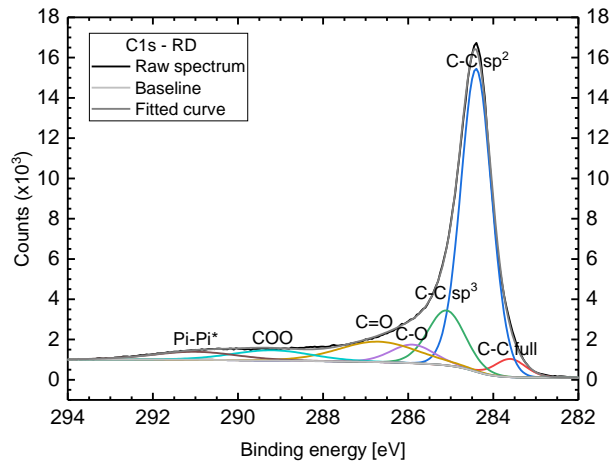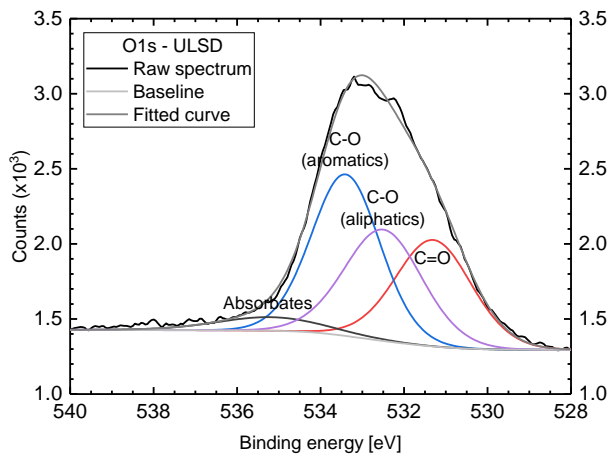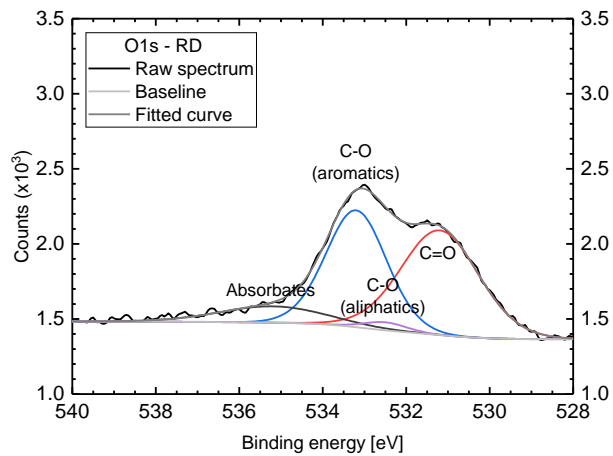
Figure 3.8. Elemental composition: ULSD (a), RD (b). Concentration of functional groups (b). C1s XPS spectra: ULSD (c), RD (d). O1s XPS spectra: ULSD (e), RD (f).

As a summary, Figure 3.9 compares the oxidation reactivity of all soot samples at 1890 min^{-1} (left) and 2410 min^{-1} (right). The mean values of the relevant parameters supporting the oxidation reactivity trend were plotted immediately above the inverse of MLRT$_{max}$ (higher values means earlier oxidation). Independently of engine speed, as RD concentration increases in the blend, the oxidation reactivity decreases. This was explained by the decrease of the ASA of soot, the increase of the degree of order of the graphene lattices, which was observed through FTIR (I$_{1640}$/I$_{2920}$) and Raman (A$_{D1}$/A$_G$, A$_{D3}$/A$_G$), and by the decrease in the interlayer distance observed with HRTEM micrographs.
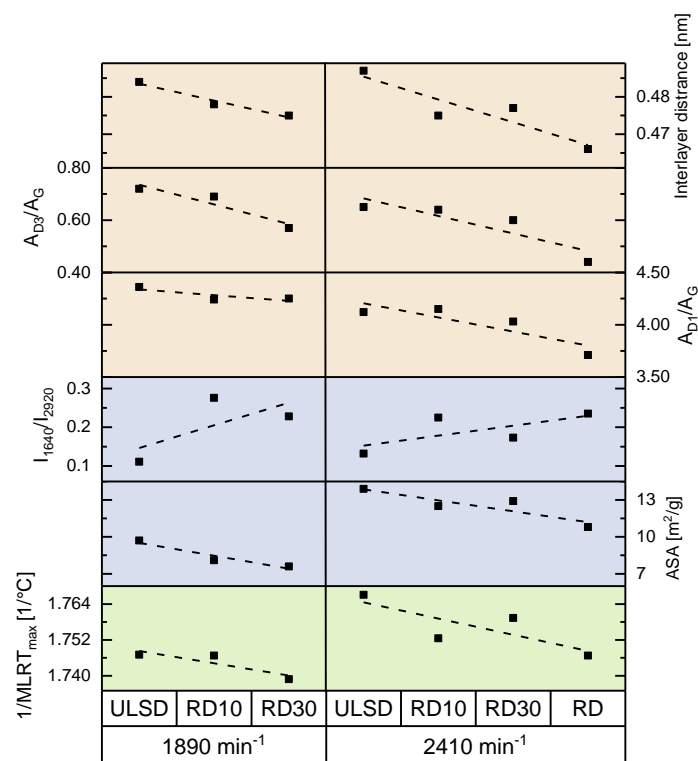
Figure 3.9. Mean values of oxidation reactivity (inverse of MLRT$_{max}$), ASA, FTIR (I$_{1640}$/I$_{2920}$), Raman (A$_{D1}$/A$_G$ and A$_{D3}$/A$_G$ ratios) and HRTEM (interlayer distance).

3.2. Results related to flame burners

3.2.1. *Stability map of the partially premixed flame burner*

A flame is stable when the flame burning velocity and fuel-air mixture flow velocity are in balance. Therefore, if any mismatch occurs between them, the flame is unable to be attached to burner rim. There are some terms associated to flame stability limits [105]: lift-off, blow-out, blow-off and flashback. Lift-off happens when the jet velocity exceeds the flame speed causing that the flame moves above the burner rim (there is a space between the burner mouth and the base of the lifted flame). If the jet velocity is further increased, the reaction may not be sustained and the flame is extinguished (blow-out). Blow-off phenomenon occurs when an attached flame is directly extinguished without lift-off stage. Finally, flashback takes place when the local flame velocity is higher than the local flow velocity resulting in the flame being pushed upstream through the burner tube. Multiple variations in flow rates of both air and fuel, allowed identified these phenomena and establish the limits of stable operation for the partially premixed flame burner used in this study. Stability maps of the PPF system were depicted for ULSD and RD (Figure 3.10). Air flow rates less than 6 L/min led to flashback phenomenon and those air flow rates higher than 10 L/min resulted in flame blow-off. A lower limit was evidenced at some equivalence ratios when the flame started to lift and then blow out. An upper limit was also identified when the flame extinguished as a consequence of poor fuel vaporization (the amount of fuel injected exceeds the vaporization capacity of the hot air stream). Compared to ULSD, the higher stoichiometric air/fuel ratio of RD, allowed reaching higher equivalence ratios for the same flow conditions. To compare the soot characteristics, an intermediate point with an air volumetric rate of 8.5 L/min and an equivalence ratio $\Phi = 1.4$ (red dot in Figure 3.10) was chosen because it is a common stable condition for ULSD and RD that produces mature soot. Table 3.6 shows the both the fuel and air flow rates used to achieve the same equivalence ratio.
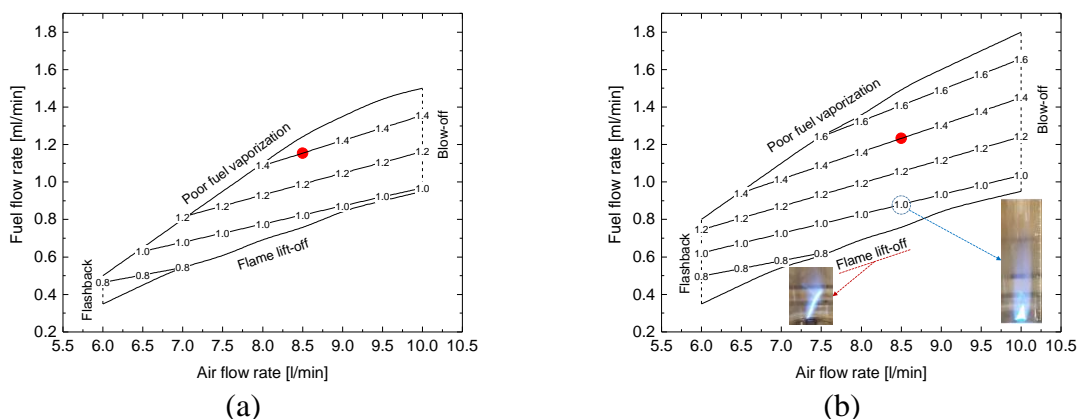

(a)   (b)

Figure 3.10. Stability map of ULSD (a) and RD (b).

Table 3.6. Experimental conditions for partially premixed flames.

Fuel	Stoichiometric air/fuel ratio[a]	Air flow rate [L/min]	Fuel flow rate [mL/min]	Equivalence ratio	C/O ratio
ULSD	14.442	8.5	1.154	1.4	0.485
RD30	14.574	8.5	1.175	1.4	0.483
RD	14.908	8.5	1.232	1.4	0.457

[a] Calculated from elemental analysis.

3.2.2. Flames description

Under conditions tested, flames have an average height of 13 cm and 4 cm for PPF and NPF, respectively. While the typical yellow region was identified in NPF, two regions were observed in PPF. A bright blue cone (which represents the premixed reaction zone) and a surrounding region consisting of unburned species that continued to burn with ambient air (diffusion zone). This second region has a blue-violet part (soot-free) and a luminous yellow zone (soot). When RD is added to ULSD, the blue-violet zone increased in PPF and the soot trail becomes narrower in both PPF and NPF (see red circles in Figure 3.11), indicating lower soot formation. It is widely accepted that if the parent fuel has aromatic compounds in its formulation, the soot emission will be higher than that of fuel with paraffinic nature [106].

(a)   (b)   (c)   (d)   (e)   (f)
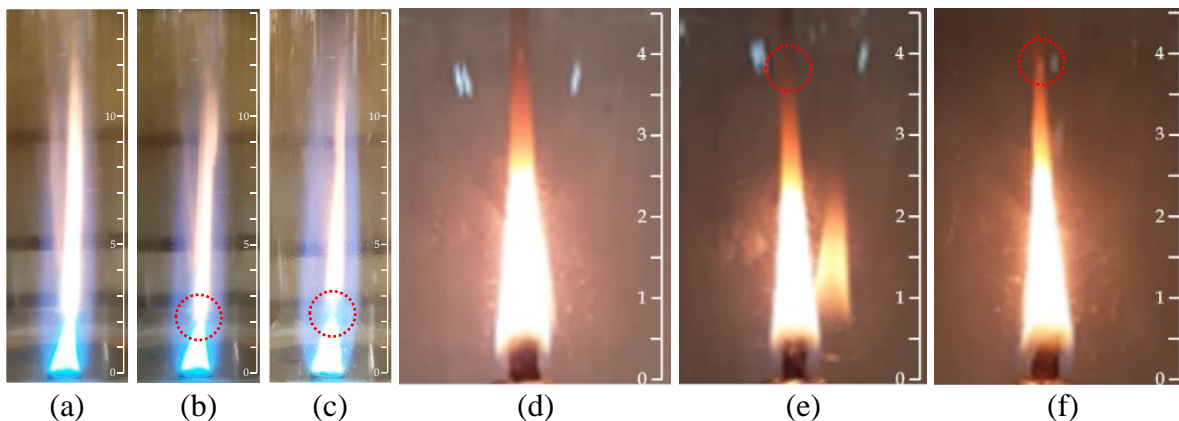
Figure 3.11. PPF of ULSD (a), RD30 (b), RD (c); and NPF ULSD (d), RD30 (e) and RD (f).

As expected, Table 3.7 shows the decrease in soot emission as RD fraction increases. Increase the paraffinic fraction from 33% (ULSD) to 53% (RD30) represents a reduction of soot mass emission of 53% and 28% in PPF and NPF systems, respectively. When neat RD was used in PPF and NPF, these reductions reached an 83% and 70%, respectively.

Table 3.7. Mass emission in flame burners.

Fuel	Partially premixed flames	Non-premixed flames
	Mass[a] (SD) [$\times 10^{-9}$ mg/cm^3]	Mass[b] (SD) [mg]
ULSD	11.19 (1.87)	17.4 (0.9)
RD30	5.27 (0.59)	12.5 (0.8)
RD	1.93 (0.32)	5.2 (0.4)

[a] Derived from mass distributions (Figure 3.14b).
[b] Mass collected in filters.

The yellow luminosity is higher for ULSD flames due to their augmented soot radiation. A lower flame temperature for ULSD flame is expected because the higher the soot concentration, the more energy is radiated by soot, which results in lower flame temperature [107]. Figure 3.12 shows the temperature of the flame at different locations in all NPF. It can be noted that the temperature profile along the height of the flame is similar for the three fuels, but it is seen that at every location, flame temperatures are higher for RD flame. Compared to ULSD, the flame temperature increased about 34 °C in average when RD30 is burned and a maximum difference of 170 °C is reached for the RD flame. Higher temperatures for paraffinic flames compared to flames produced by fuels with aromatic formulation have been reported. Velasquez et al. [108] using an inverse diffusion flame burner showed that, independently of the flame height, hexane flame temperature was in average 300 °C above of the diesel surrogate flame (which contained about 20 %vol. of aromatics compounds). Botero et al. [109] reported that n-heptane non-premixed flame exhibited higher flame temperature compared to n-hexane/toluene blends.
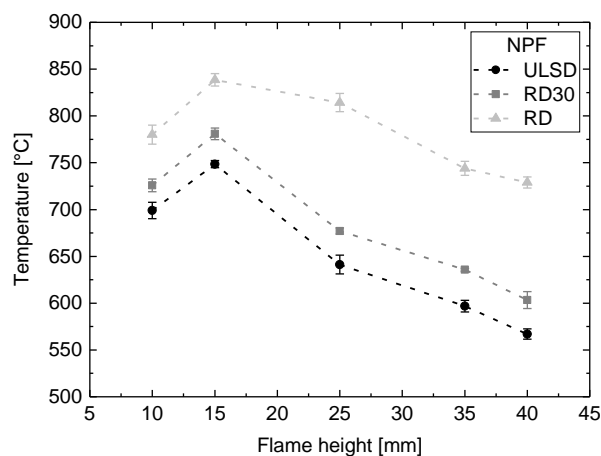
Figure 3.12. Flame temperature of NPF

3.2.3. Primary particle size and particle size distribution

Figure 3.13 displays the d_{pp} estimated from TEM images of PPF and NPF samples. Independently of the burner type, the addition of RD into ULSD led to a decrease in d_{pp}. In PPF system, the difference in d_{pp} is about 3 nm when neat RD is used, while in NPF burner the d_{pp} decrease 17 nm (see table below the Figure 3.13). The reduction in the size of primary particles could be associated to i) the fact that paraffinic fuels must follow a much more complex and slower path under similar residence time to produce the first aromatic ring compared to aromatic fuels [101] hindering the particle enlargement, and ii) the high temperature of RD flames cause a highly oxidizing environment that shrinks the particles. It can be also noted that PPF generated smaller primary particles compared to NPF. About 1.5 to 2 times in size is the difference when the same fuel is burned but in different burner configuration. This result might be related to the shorter residence time in PPF that impedes the surface growth (in contrast with the extended combustion duration in diffusion flames that favors particle development).
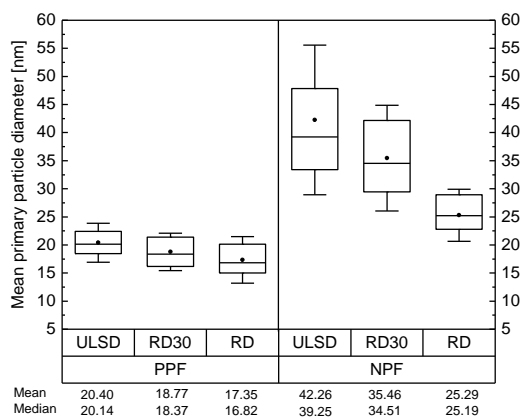

	ULSD	RD30	RD	ULSD	RD30	RD
		PPF			NPF	
Mean	20.40	18.77	17.35	42.26	35.46	25.29
Median	20.14	18.37	16.82	39.25	34.51	25.19

Figure 3.13. Mean primary particle diameter (d_{pp}) of flame samples.

Figure 3.14a shows the particle number size distribution of the samples gathered in PPF. The size distributions shows that the addition of RD into ULSD reduces the mean size of the emitted particles. It seems to be that the overall lower emission level of RD leads to less chance for agglomeration. PSD shows that the number of particles smaller than 27 nm is higher for RD flames, but the number of particles larger than 33 nm is higher for ULSD (Figure 3.14a). PSD results of Botero and co-workers demonstrated that paraffins fuels produced smaller particles than aromatics [109] and cycloalkanes [110] (these compounds represent about two thirds of diesel fuel composition). Mauss et al. [111], using a PPF burner (counterflow configuration), showed that flames with lower C/O ratio produced smaller particles, which is also in agreement with the results presented here (see Table 3.6).
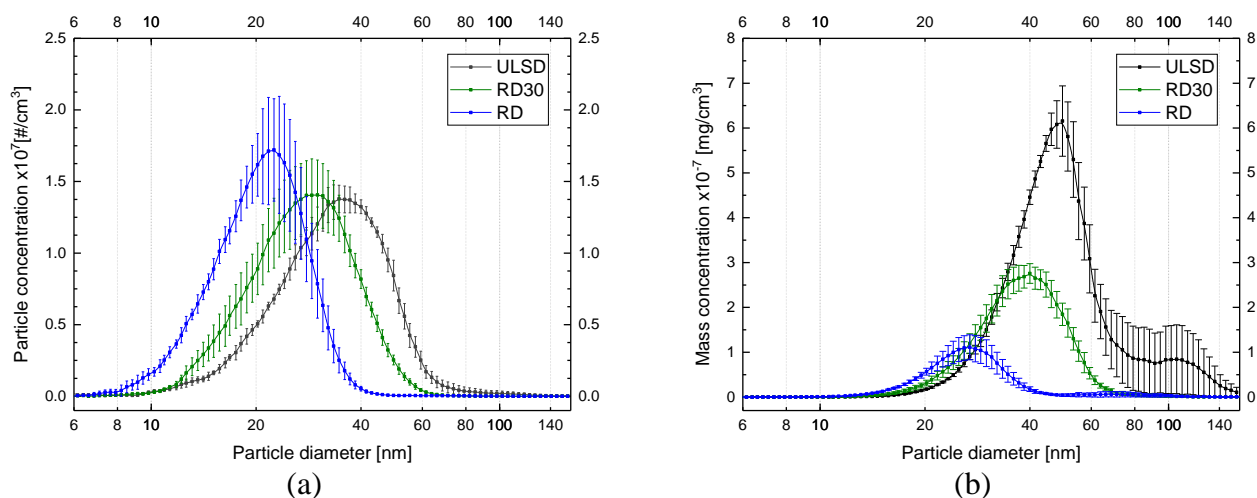
Figure 3.14. Particle number (a) and particle mass (b) size distributions for PPF.

It is important to mention that this high concentration of ultra-fine particles is compensated with lower mass emission of RD (Figure 3.14b). Ng and collaborators [112], using a single-cylinder diesel engine, reported that SunDiesel (a paraffinic fuel produced through biomass-to-liquid technology) emitted much more ultra-fine particles (< 70 nm) compared to diesel fuel. Soriano et al. [62] showed that, in comparison with diesel fuel, the combustion of GTL and farnesane (a paraffinic fuel derived from sugar cane) in a diesel engine, led to higher number concentration of particles smaller than 150 nm. In a recent study, conducted by Shukla et al [113], higher concentration of nucleation mode particle was evidenced for RD at 2000 bar of engine rail pressure, compared to diesel fuel. They explain that higher cetane number of RD resulted in lower accumulation mode (this implies smaller surface area for adsorption of organic species that may form nucleation mode), which ultimately can increase the nucleation mode in the exhaust.

3.2.4. Soot nanostructure

Representative spectra of the flame samples are plotted in Figure 3.15 (all the Raman spectra can be found in Appendix E). At first sight it can be see the clear influence of both fuel composition (Figure 3.15a) and burner type (Figure 3.15b) on Raman spectra. For better comparison, Figure 3.16 depicts the area ratios of Raman bands related to structural defects, i.e., A_{D1}/A_G, A_{D3}/A_G and A_{D4}/A_G (values are reported in Table E1 of Appendix E). As mentioned above, the presence of D1 and D3 bands implies, respectively, disordered graphitic structures and amorphous carbon in soot, while D4 account for ionic impurities or C=C stretch like those of polyene-like structures [85].
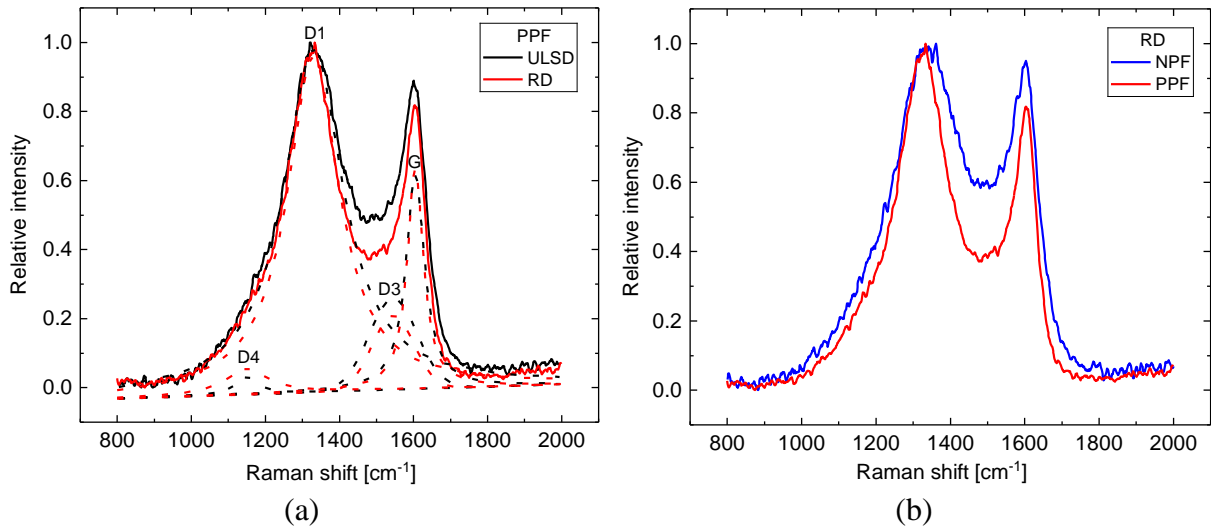
44

Figure 3.15. Raman spectra: effect of fuel (a) and effect of flame type (b).

Regardless the flame burner, the decreasing trend in all the mean area ratios (except for A_{D4}/A_G in PPF) indicates that the addition of RD into ULSD produces a soot with a more inner ordered structure. Additionally, when the same fuel was burned using different flame configurations, a clear reduction in every area ratio indicate that compared to NDF, the soot samples gathered from PPF presented more graphite-like structure (reduced A_{D1}/A_G), less amorphous carbon content (decrease in A_{D3}/A_G) and less ionic impurities (low A_{D4}/A_G), thus, a higher internal degree of order. It is believed that both findings are consequence of high-temperature environments (based on the conceptual model of Marsh and Griffiths [86]). It has been stated that RD flame temperature is higher than that of ULSD flame (flame sootiness markedly affect the flame temperature due to heat loss mechanism). Similarly, compared to NPF system, higher flame temperatures are expected in PPF burner not only because of its less-sooting nature, but also due to relatively more complete combustion caused by the supplied air (in opposite to incomplete combustion in NPF).
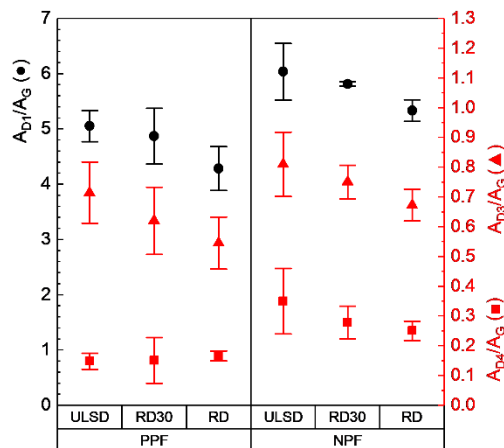

Figure 3.16. Raman peak area ratios of the flame samples.

45

3.2.5. Soot morphology

TEM images of the agglomerates of all flame samples are shown in Figure 3.17. Regardless the fuel and burner configuration, PM exhibited typical sphere chain-like structures but with complex networks of branches. In contrast to the NPF-derived agglomerates, the branches of PPF samples are composed of a high number of primary particles, especially those generated by RD. As mentioned in the methodology section, long branches of the PPF agglomerates are overhanging from the lacey carbon supports. This led to a high shakiness of the particles that impeded taking proper HRTEM micrographs of the primary particle for fringe analysis. Therefore, only HRTEM images from NPF samples were obtained for fringe analysis.

(a)	(b)	(c)
(d)	(e)	(f)
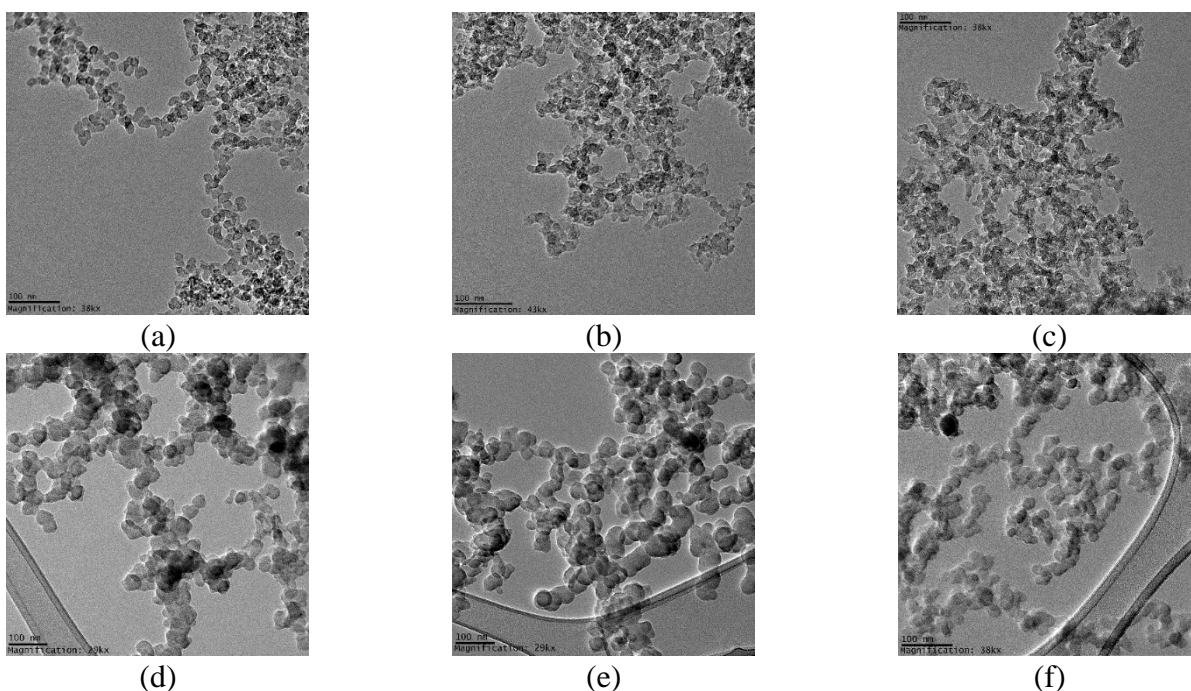
Figure 3.17. TEM images of aggregates gathered in PPF and NPF burners. PPF: ULSD (a), RD30 (b) and RD (c). NPF: ULSD (d), RD30 (e) and RD (f).

Representative HRTEM images of the NPF samples are displayed in Figure 3.18. All these primary particles exhibited the typical shell/core nanostructure which consists in an amorphous or isotropic phase (where graphene layers are randomly oriented in a central core), and a graphite-like crystalline domains or nematic phase (where the graphene layers are oriented parallel to the external surfaces in an outer shell) [75]. Qualitative evaluation of these micrographs shows that, compared to RD30 and RD particles, ULSD particle have more amount of arranged fringes in the shell region (see red arrows in Figure 3.18), indicating higher surface growth by progressive layer deposition.
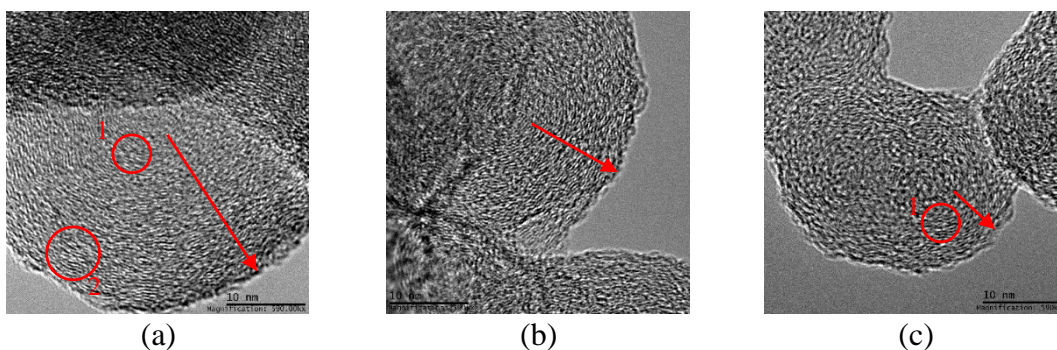
Figure 3.18. HRTEM images of NPF particles: ULSD (a), RD30 (b) and RD (c).

Figure 3.19 displayed the graphs (with box plots and lines) obtained from fringe analysis of particles collected in NPF burner. On the one hand, the box plots show the medians, standard deviations (whiskers), 25% and 75% percentiles (upper and lower limit of the box) and means (dots) of the interlayer distance, fringe length and tortuosity (curvature due to defects in the graphene layers). On the other hand, the lines depict the relative frequency of the calculated values. Increase the paraffinic content in the fuel, cause a decrease in interlayer distance (Figure 3.19a) which is associated to the high-graphitized nature of the particles. Compared to ULSD soot, the RD produce particles with shorter (Figure 3.19b) and more curved fringes (Figure 3.19c). This is in agreement with ref. [69] where argued that high flame temperature produce a high oxidizing surrounding that reduces the fringe length and increases the tortuosity. The carbon lamellae is bent during oxidation, not only due to disorder introduced by oxygen absorption, but also because of the formation of intermediate 5-member ring species which results in local curvature [114]. For RD particles, it can be observed in Figure 3.19c an increase in the relative concentration of fringes with tortuosity between 1.12 and 1.30 at the expense of the reduction of the percentage of less-curved fringes (tortuosity ~1.1). In addition, it is believed that graphene layers are expected to be more curved, as they are located closer to the particle center. Thus, smaller particles (like those produced by RD) have higher concentration of fringes with high curvature due to their proximity to the inner core (fringes in red circle 1). In contrast, larger particles (like those generated by ULSD) have much more fringes with lower curvature at the outer edge of the particle (fringes in red circle 2).
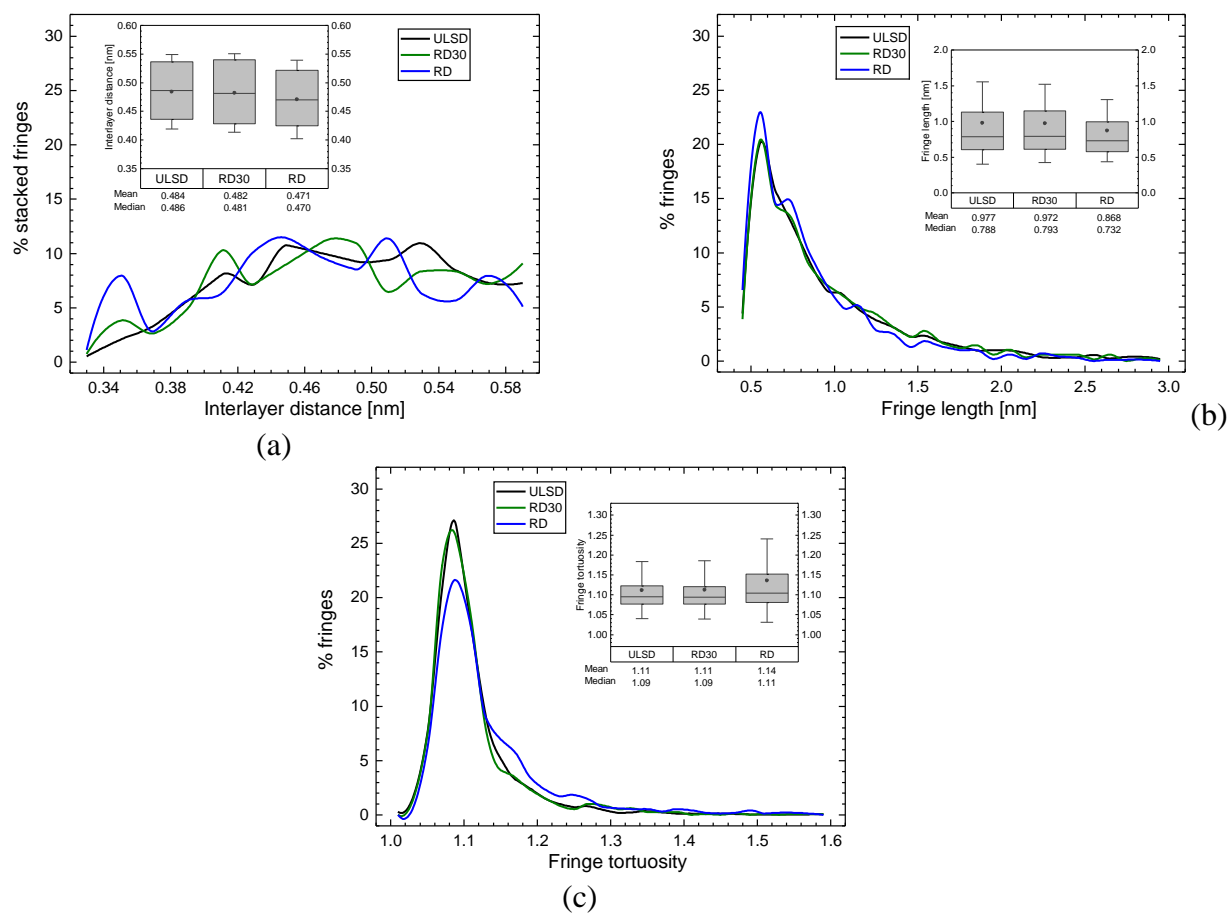
Figure 3.19. Fringe analysis of particles collected in NPF burner. Interlayer distance (a), fringe length (b) and fringe tortuosity (c).

3.2.6. Functional groups

Figure 3.20 displays the fingerprint region of infrared spectra of all PM samples. It can be seen that, although NPF spectra shows more intense signals compared to PPF spectra (possibly due to more organic material in the NPF samples), both groups of spectra shows an increase of the intensities of the functional groups related to CH_3 plane deformations (1380 cm^{-1}) of aliphatic groups and C=C stretching vibration (1640 cm^{-1}) when RD is used (see Table 3.8). The fundamental pathway for the decomposition of large paraffins proposed by Zhang et al. [100, 101] involves either hydrogen abstraction or thermal decomposition to form alkyl radicals, each of which decomposes via β scission to form alkyl radicals and olefin species. Based on this mechanism, it is likely that the combustion of RD (composed of higher paraffins, C_{15}-C_{18}) yielded CH_3 radicals and olefinic C=C compounds that were subsequently condensed onto the particle surface. On the other hand, the addition of RD raised the flame temperature and thereby, increased the condensation of aromatic systems on the surface of particles (the soot structure become more ordered) [102]. No appreciable changes were found for oxygenated functionalities at 1735 cm^{-1} and in the region of 1000-1300 cm^{-1}.
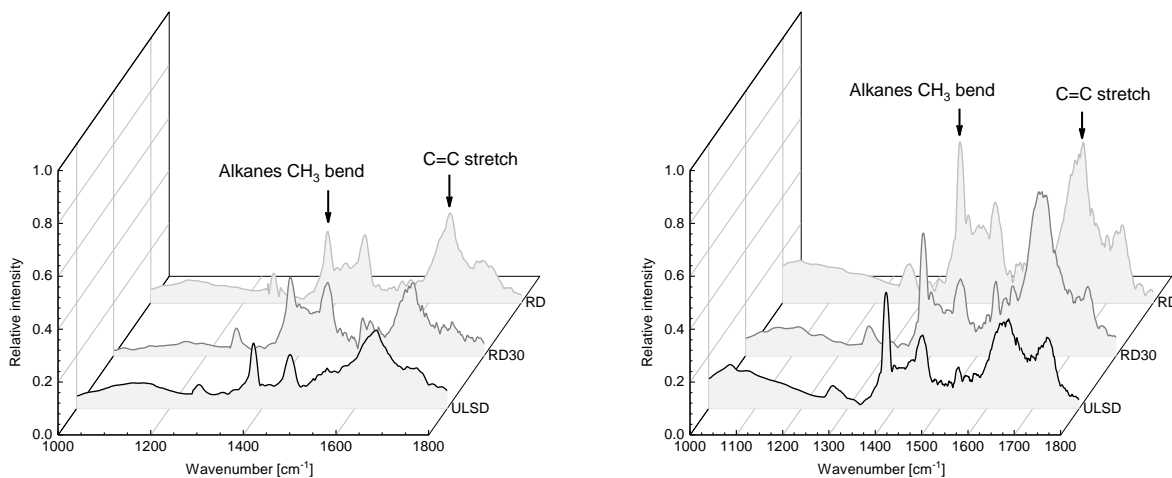
Figure 3.20. Infrared spectra of soot from PPF (a) and NPF (b).

Table 3.8. Relative intensities of infrared signals of flame samples.

Burner	Fuel	Wavenumber [cm^{-1}]	
		1380	1640
	ULSD	0.245	0.295
PPF	RD30	0.296	0.274
	RD	0.270	0.339
	ULSD	0.433	0.334
NPF	RD30	0.463	0.601
	RD	0.610	0.607

Note: Data are normalized to the intensity of the 2920 cm^{-1} signal.

3.2.7. Comparison between engine soot and flame soot

The study conducted in the automotive diesel engine (section 3.1) suggests that the addition of RD into ULSD promotes smaller primary particles with more ordered internal nanostructure. Various relationships can be drawn when comparing some characteristics identified for particles gathered in flame burners with those evaluated in the engine-derived samples. In this section, mean primary particle size (calculated with TEM images), soot nanostructure (using the fringe features obtained from HRTEM micrographs and the Raman parameters), and the chemical functional groups (from the infrared analysis) are discussed and only data related with neat RD and ULSD are presented. Figure 3.21 shows the mean diameter of the primary particles as a function of both fuels and combustion environment. According to this graph, the size of the particles were ranged between ~17 nm and ~55 nm for ULSD fuel and between ~13 nm and ~33 nm when neat RD was burned. The reduction of particle size was slightly more evident when PPF system is used. An interesting fact could be also noted here: particles generated in diesel engine possess intermediate diameters between those generated in PPF and NPF. This could be associated with the hybrid nature of the diesel combustion consisting of an initial combustion phase controlled by a partially premixed mixture inside the cylinder and a later

49

phase characterized by a diffusion-driven process. This finding also might support the fact that during diesel combustion, some small particles are generated in the premixed burn (in the well-mixed section of air and fuel vapour) and they could grow as they pass through the combusting plume towards the enveloping diffusion flame [115].
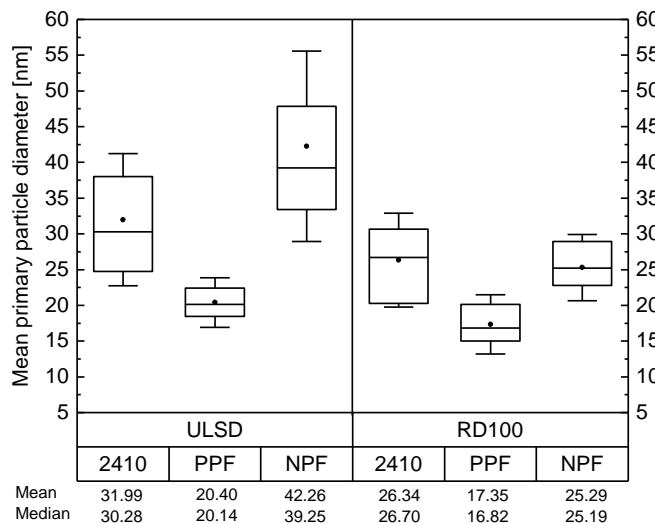

	ULSD			RD100		
	2410	PPF	NPF	2410	PPF	NPF
Mean	31.99	20.40	42.26	26.34	17.35	25.29
Median	30.28	20.14	39.25	26.70	16.82	25.19

Figure 3.21. Mean primary particle diameter of
samples from different combustion systems.

Figure 3.22 displays the results of the fringe analysis performed to engine soot and NPF-derived soot. While fringe length results (Figure 3.22a) are similar for ULSD and RD, although small, a relative more curved fringes (Figure 3.22b) and more pairs of fringes with a decreased separation (Figure 3.22c) were generated when both systems were fueled with neat RD. No effect was observed in the fringe features when the fuel is burned on different combustion system, in spite of the big difference in the pressure and turbulence at which combustion takes place. Similar result was reported by Jaramillo et al. [116], who studied the soot nanostructure of partially oxidized soot at 1, 10 and 40 atm. Their lattice fringe analysis algorithm showed that increasing pressure caused no apparent changes in the nanostructure (fringe length or tortuosity) for the samples produced by non-oxygenated fuels (m-xylene, n-dodecane and m-xylene/n-dodecane blend) in a premixed flat flame burner.
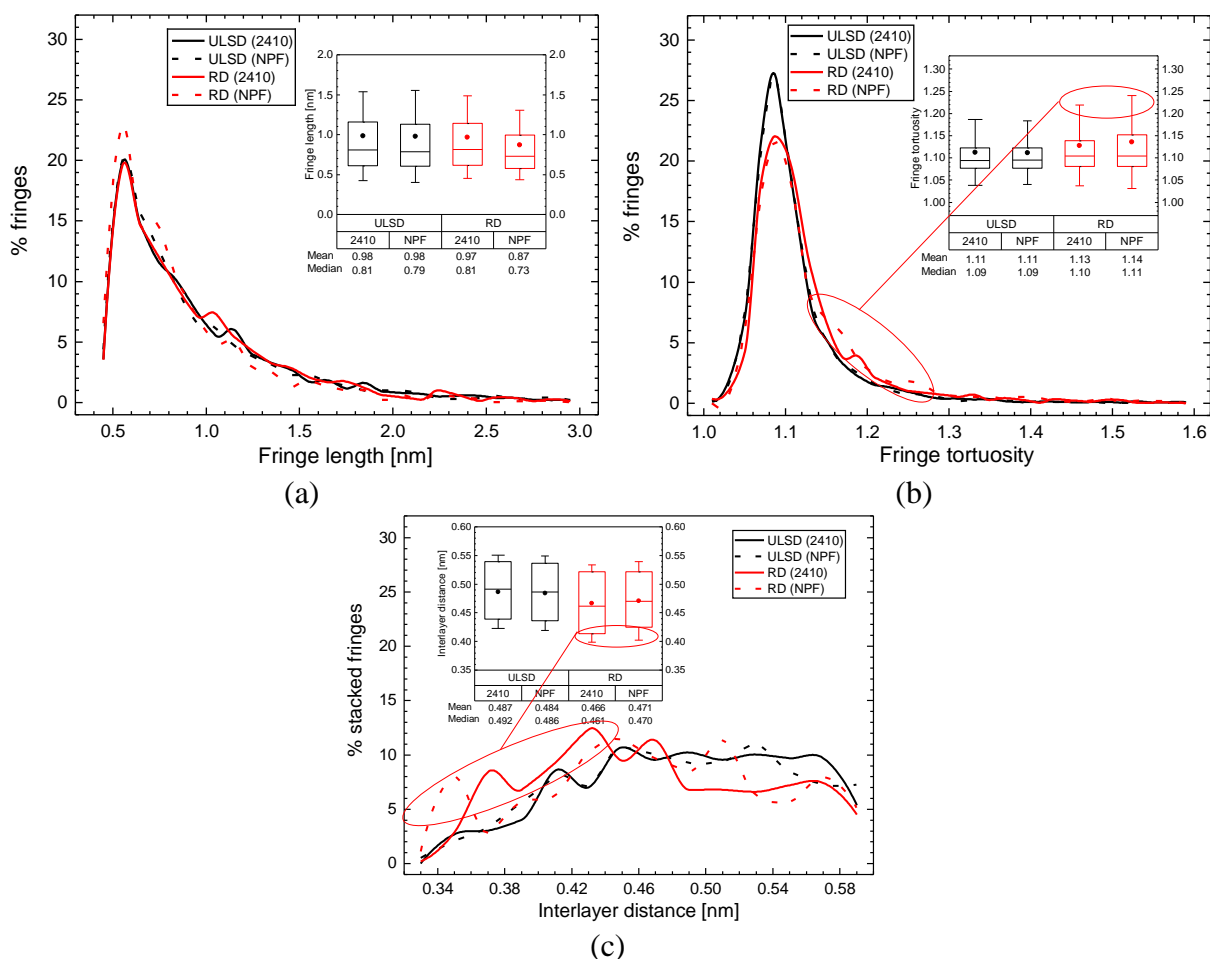
Figure 3.22. Fringe parameters of samples from different combustion system: fringe length (a), fringe tortuosity (b) and interlayer distance (c)

Raman spectra in Figure 3.23 reveal an influence of the combustion system in the structural order of soot particles. It is clear to see that independently of the fuel, the bands related to plane defects in the Raman shift suffer an appreciable reduction in their areas (see Table E1) and the G band become sharper (which implies that the particle increase the graphitic domains in its internal structure) as the combustion goes from a diffusion-like process (green spectra) to a partially premixed conditions (red spectra).

Area ratios extracted from Raman spectra through multiple peak decomposition process are plotted in Figure 3.24. The mean of A_{D1}/A_G and A_{D3}/A_G area ratios from engine samples are the lowest, indicating better graphite-like structure with less amorphous domains compared to those generated in flame configuration. This is not surprising because, in contrast to the combustion at atmospheric pressure in flame burners, the samples gathered at the engine exhaust were subjected not only to high temperatures but also to a high pressure inside the cylinder, increasing their degree of graphitization.

51

NPF samples showed the higher degree of structural disorder (as indicated by their larger A_{D1}/A_G and A_{D3}/A_G values), no matter the fuel tested. This result could be anticipated based on the temperature at which the particles are formed, that is expected to be the lowest among the tested combustion systems (due to incomplete combustion conditions and to higher sooting nature of wick-fed flame burner).

(a)   (b)
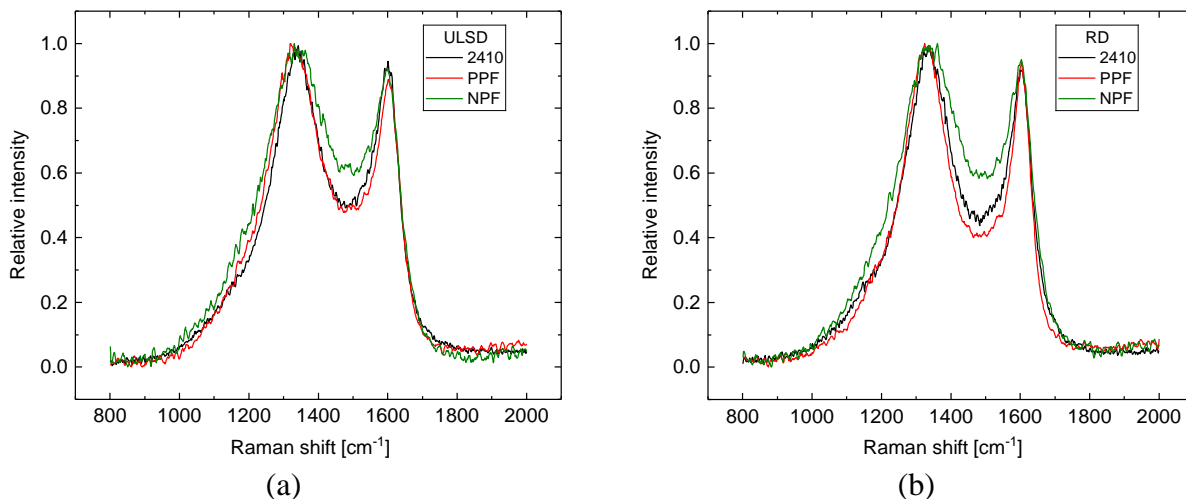
Figure 3.23. Raman spectra of samples from different combustion systems: ULSD (a) and RD (b).
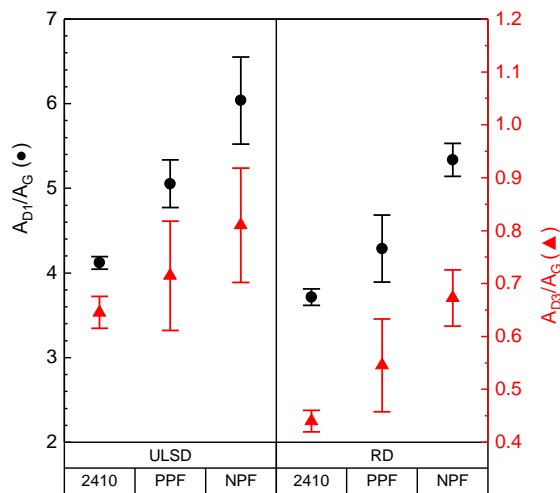
Figure 3.24. Raman bands area ratios of samples from different combustion systems.

Table 3.8 shows the infrared signals of the samples collected under the three different combustion conditions. Independently of the combustion system, it can be observed that functional groups associated with C=C stretch and aliphatic CH_3 bend are more intense when RD is burned. The reasons for this result were discussed above in section 3.6. However, the relative intensity of oxygenated groups (1240 and 1735 cm^{-1}, see Table 3.8) is higher for engine samples, regardless the fuel examined. This finding is related to the lean conditions in which diesel combustion occurs. High amount of

52

oxygen (due to excess of air) inside the cylinder reacts to produce oxidized species onto the particle surface.

Table 3.8. Relative intensities of infrared signals of samples from engine and flames.

Fuel	System	Wavenumber [cm^{-1}]			
		1240	**1380**	**1640**	**1735**
ULSD	2410	0.138	0.457	0.102	0.302
	PPF	0.090	0.245	0.295	0.153
	NPF	0.085	0.433	0.334	0.269
RD	2410	0.225	1.297	0.207	0.386
	PPF	0.112	0.270	0.339	0.159
	NPF	0.148	0.610	0.607	0.294

Note: Data are normalized to the intensity of the 2920 cm^{-1} signal.

The results suggest that the "fine nanostructure" of soot (i.e., fringe parameters, evaluated by HRTEM) is only dominated by the fuel composition, but the surface chemical composition and the "bulk nanostructure" of the soot (i.e., amorphous and graphitic domains, quantified through Raman parameters) are markedly affected by both the fuel formulation and the combustion system. In contrast to this last finding, the work conducted by Commodo et al. [117] in a coflow methane−air diffusion flame, showed that increasing the pressure of the system from 10 to 20 bar did not affect the nanostructure of the gathered soot. Instead, their Raman results indicated that residence time appeared to be the governing factor of soot nanostructure. The discrepancy with the present work might be related to the fact that they did not compare with atmospheric pressure, which could exhibit significant changes in the soot nanostructure.

Chapter 4
CONCLUSIONS AND RECOMMENDATIONS FOR FUTURE WORKS

4.1. Conclusions

The present work uses three different combustion systems to evaluate the impact of renewable diesel (RD) on the soot characteristics. Neat renewable diesel (RD), ultra-low sulfur diesel (ULSD), and their volumetric blends of RD10 and RD30 were used to elucidate how the paraffinic nature of RD affects the internal structure, morphology and chemical composition of the particulate matter. The first evaluation was performed on particles collected at the exhaust of an automotive diesel engine running at two stationary modes (1890 min^{-1} and 2410 min^{-1} at 95 Nm). In order to support the results derived from engine experiments, a second characterization was carried out on particles generated with the same fuels using partially premixed and non-premixed flames.

Under the specific experimental arrangement conducted in diesel engine and flame burners, it can be concluded that the oxidation reactivity of the PM produced by the fuels in the diesel engine was slightly affected by fuel composition (the $MLRT_{max}$ was 6.6 ℃ lower for ULSD than neat RD). A minor trend to decrease the oxidation reactivity of the soot was observed with the increase of renewable diesel into diesel fuel blend, which was in agreement with the low active surface area of the soot, as well as with the high degree of order of the graphene layers of the soot. Although small, high engine speed generated a more reactive soot. The diameter of the primary particle and the fractal dimension of the aggregates tend to decrease with both, renewable diesel concentration and engine speed. From this engine configuration and specific experimental setting, it can be expected that the use of RD blends would not markedly affect the performance of aftertreatment devices like diesel particulate filters.

In addition, analysis carried out on flame soot confirmed that the addition of RD into ULSD produced more graphitized particles. The high degree of order (determined by Raman parameters) was in agreement with the interlayer distance (performed on HRTEM micrographs) and with the intensity of C=C stretch in FTIR spectra. Particle size distributions measured in PPF corroborated the decrease of particle size with RD concentration, but also revealed higher number concentration of ultrafine particles. Concerns about the smaller and numerous particles generated by RD, could be compensated by its reduced mass emission (over 70% when neat RD is used). Although lattice arrangements seemed

to be unaffected by combustion conditions, the structural defects (e.g., due to functional groups) in the basal plane and edges of individual graphene layers were impacted, for instance, by the pressure and turbulence of the system (elevated in engine vs atmospheric in flame burners).

4.2. Recommendations for future works

From the present investigation, various tasks are recommended in order to transcend the limitations of this work:

- Extent the PM characterization to particle toxicity.

The assessment of the genotoxicity and mutagenicity of the PM extracts is an important research topic nowadays. It is highly recommended to complement the soot characterization conducted here with an evaluation of the biological impact of the particulate emitted by renewable diesel.

- Study of the influence of equivalence ratio on soot characteristics.

Complex fuels are rarely addressed in fundamental studies. The partially premixed flame burner used in this work enables the possibility of using diesel-like fuels to evaluate, for instance, the effect of equivalence ratio on soot characteristics.

Appendix A
Related to renewable diesel production

The renewable diesel production was carried out in a facility of Route N Innovation Center at Medellín, Antioquia, Colombia. The process, conducted under the guidelines of Procesos Químicos Industriales (PQI) research group, yielded about 30 liters of pure renewable diesel. The protocol of the fuel production claimed for a quick in-situ test (ATR and GC) to evaluate the quality of every produced batch. Characterization of the fuel was performed by PQI research group in conjunction with Crudos y Derivados Lab (UNalMed).

| (a) | (b) | (c) | (d) |
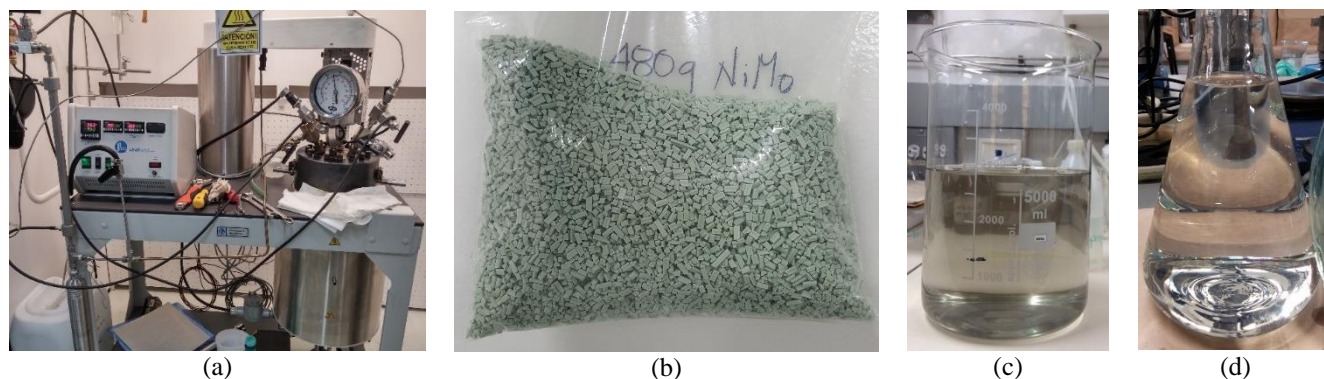
Figure A1. High pressure reactor used for renewable diesel production (a). Catalyst used for hydrotreating palm oil (b). Renewable diesel before (c) and after (d) filtering particles of catalyst.

Table A1 shows the GC profile of the crude vegetable palm oil used for the production of renewable diesel fuel. Main fatty acids of this oil are palmitic C16:0 (43.3 %w/w) and oleic C18:1 (40.7 %w/w). In addition, it can be seen fatty acids with double bonds like oleic, linoleic and linolenic. The production of renewable diesel involves three reactions: hydrogenation (saturation of double bonds), hydrocracking (breaking of triglycerides in monoglycerides, diglycerides and fatty acids) and deoxygenation which removes oxygenated groups from the fatty acids structure. Deoxygenation occurs by three simultaneous chemical pathways: hydrodeoxygenation (HDO, consumes H_2 and oxygen is eliminated by H_2O formation), decarbonylation (DCN, uses H_2 and oxygen is removed in the form of CO and water) and decarboxylation (DCX, oxygen removal by producing CO_2). HDO does not produce carbon loss but DCN and DCX produce n-alkanes with one carbon atom less than the parent fatty acid. For palm oil used here, DCX and DCN converts C16 and C18 into C15 and C17 compounds. Table A2 displays the chemical composition of the renewable diesel produced from palm oil. Figure A2 shows the possible routes followed in this fuel production.

Table A1. Chemical composition of crude palm oil.

Type of fatty acid	%w/w
Lauric (C12:0)	0.2
Miristic (C14:0)	1.01
Palmitic (C16:0)	**43.3**
Palmitoleic (C16:1)	0.15
Heptadecanoic (C17:0)	0.16
Estearic (C18:0)	**4.53**
Oleic (C18:1)	**40.7**
Linoleic (C18:2)	**9.21**
Linolenic (C18:3)	**0.17**
Eicosanoic (C20:0)	0.4
Eicosenoic (C20:1)	0.18

Table A2. Chemical composition of renewable diesel.

Hydrocarbon	%w/w
< C15 (linear)	2.5
C15 (linear)	**29.4**
C16 (linear)	**13.6**
C17 (linear)	**38.4**
C18 (linear)	**12.1**
C19 (linear) and others	4

C16 fatty acids **43.45** %w/w
- DCN + DCX → **29.40** %w/w C15 (linear)
- HDO → **13.60** %w/w C16 (linear)
- Hydrocracking → **0.45** %w/w

C18 fatty acids **54.61** %w/w
- DCN + DCX → **38.40** %w/w C17 (linear)
- HDO → **12.10** %w/w C18 (linear)
- Hydrocracking → **4.11** %w/w
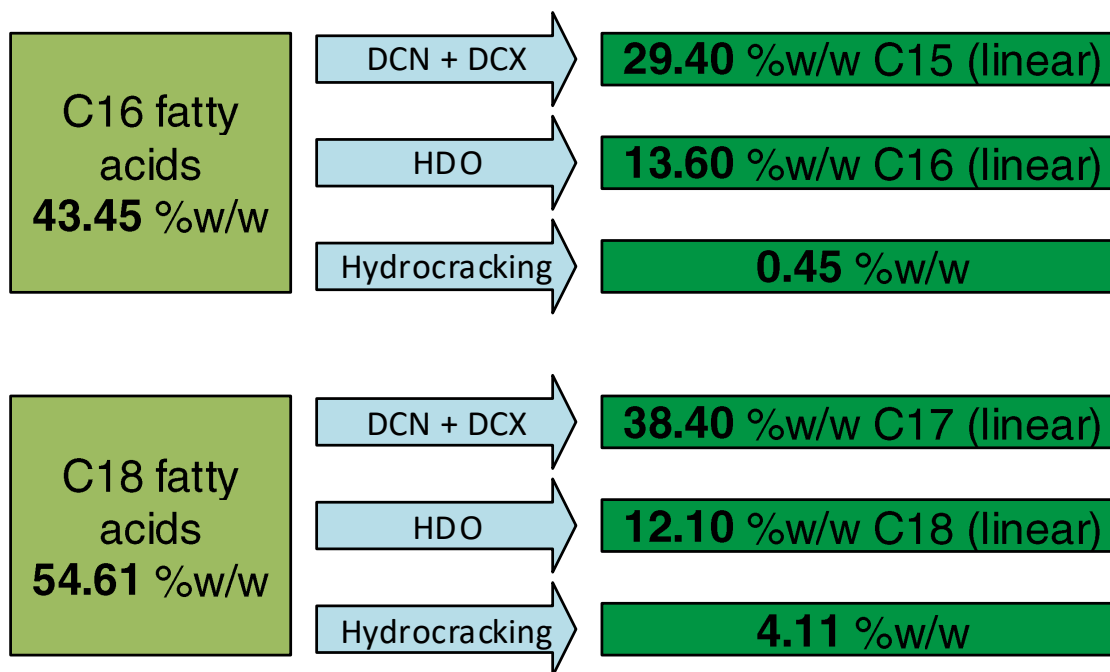
Figure A2. Conversion pathways of palm oil compounds.

Appendix B
Related to flame burners

Figure B1 shows the sequence of heating tapes wrapping the tube and the components of the burner for partially premixed flames.

(a)   (b)   (c)

(d)   (e)   (f)
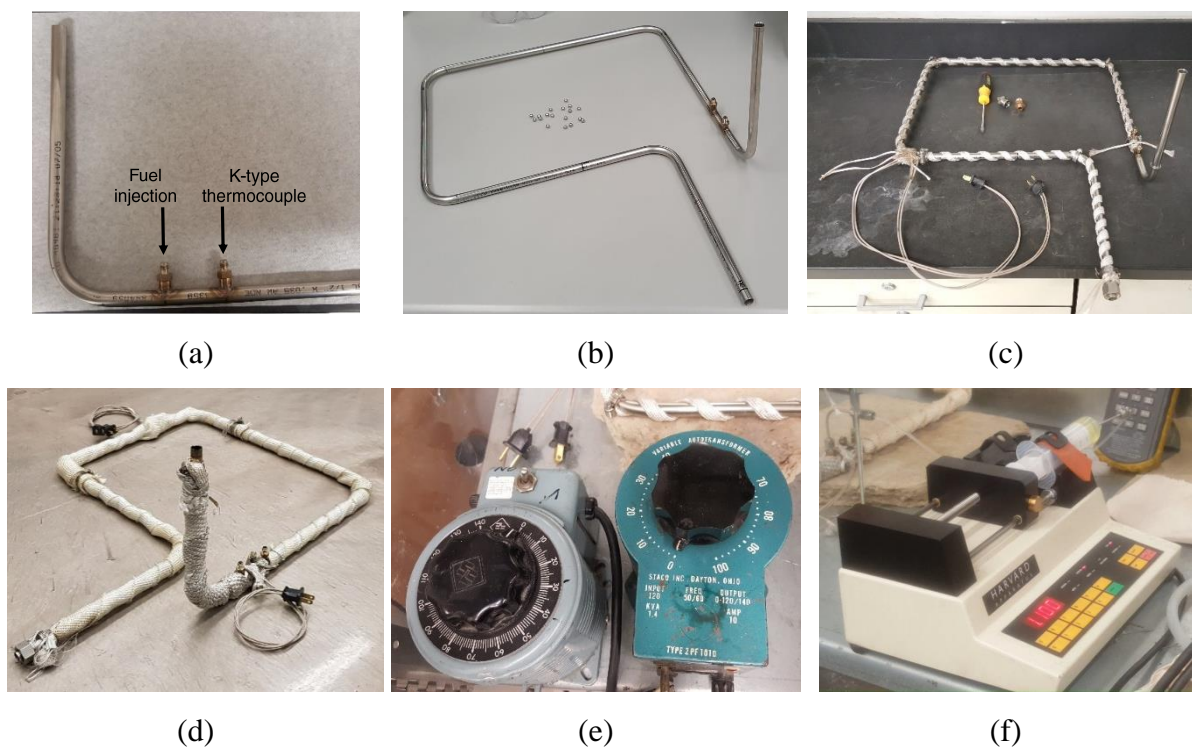
Figure B1. Components of the partially premixed flame burner.
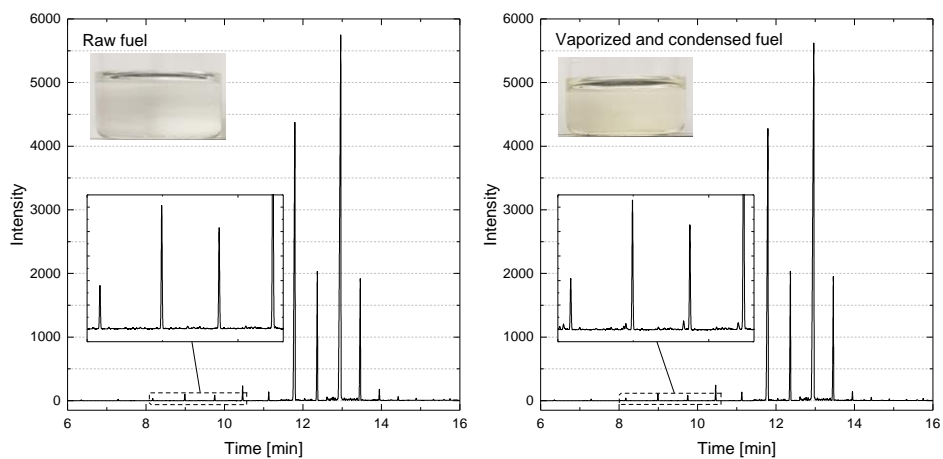
Figure B2. GC profiles of raw RD (left) and vaporized RD (right).
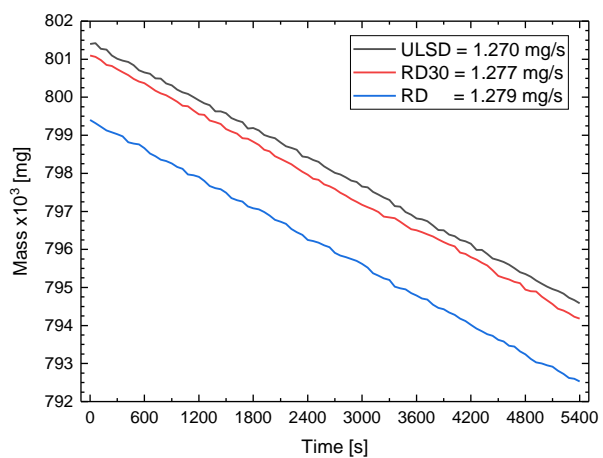
Figure B3. Non-premixed flames: fuel flow rate measurement (a) and fuel flow rate (b)

Appendix C
Related to sampling procedure

(a)	(b)	(c)	(d)
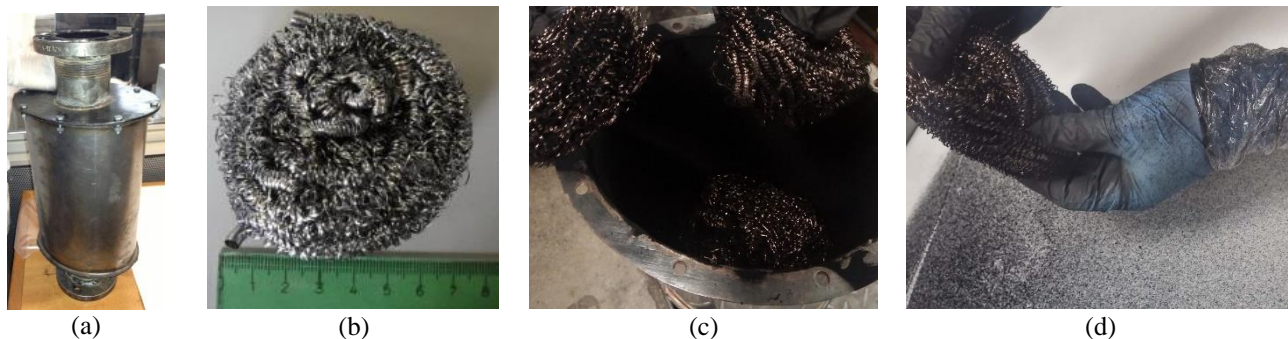
Figure C1. Stainless steel cylindrical case for sampling in diesel engine (a). Stainless steel mesh (b). Mesh with samples (c). Detail of mesh shaked (d)
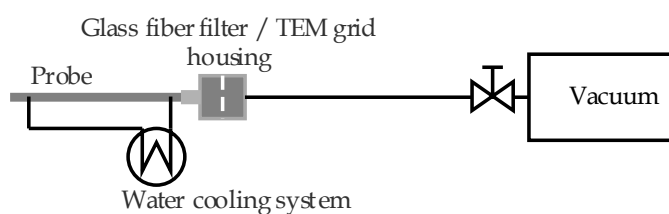
Figure C2. Water-cooled stainless steel probe for sampling in flame burners.

Appendix D
Related to thermogravimetric analysis

Table D1. Programs for thermogravimetric analysis.

Steps	Proximate analysis and soot oxidation	Active surface area
1	Start with high purity N_2 (100 mL/min)	Start with high purity N_2 (100 mL/min)
2	Ramp 5 °C/min to 30 °C	Ramp 5 °C/min to 30 °C
3	Isothermal for 30 min	Isothermal for 30 min
4	Ramp 10 °C/min to 650 °C	Ramp 10 °C/min to 650 °C
5	Isothermal for 60 min	Isothermal for 60 min
6	Equilibrate at 100 °C	Ramp 5 °C/min to 200 °C
7	Isothermal for 30 min	Change to zero air (100 mL/min)
8	Change to zero air (100 mL/min)	Isothermal for 480 min
9	Ramp 1 °C/min to 650 °C	Change to high purity N2 (100 mL/min)
10	Isothermal for 30 min	Isothermal for 90 min
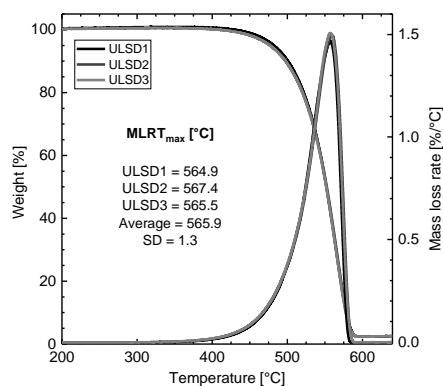
Figure D1. Standard deviation of MLRT$_{max}$

Table D2. Proximate analysis results.

Speed	Fuel	Mass before devolatilization [mg]	Mass after devolatilization [mg]	Mass after oxidation [mg]	Volatile [%]	Fixed carbon [%]	Ash [%]
1890	ULSD	2.9815	2.7464	0.0609	7.9	90.1	2.0
	RD10	3.0513	2.7994	0.0357	8.3	90.6	1.2
	RD30	3.0397	2.8245	0.0352	7.1	91.8	1.2
2410	ULSD	3.0526	2.8106	0.0706	7.9	89.8	2.3
	RD10	3.0845	2.8344	0.0667	8.1	89.7	2.2
	RD30	3.0528	2.7807	0.0344	8.9	90.0	1.1
	RD	3.0634	2.8320	0.0361	7.6	91.3	1.2

Table D3. Active surface area results.

Speed	Fuel	Mass before oxygen treatment [mg]	Mass after oxygen treatment [mg]	Chemisorbed oxygen	ASA [m^2/g]
1890	ULSD	2.6997	2.7081	0.0031	9.7
	RD10	2.6530	2.6599	0.0026	8.1
	RD30	2.6421	2.6485	0.0024	7.6
2410	ULSD	2.7118	2.7239	0.0045	13.9
	RD10	2.7640	2.7748	0.0039	12.3
	RD30	2.7548	2.7662	0.0041	12.9
	RD	2.7356	2.7450	0.0035	10.8

Appendix E
Related to Raman spectroscopy analysis
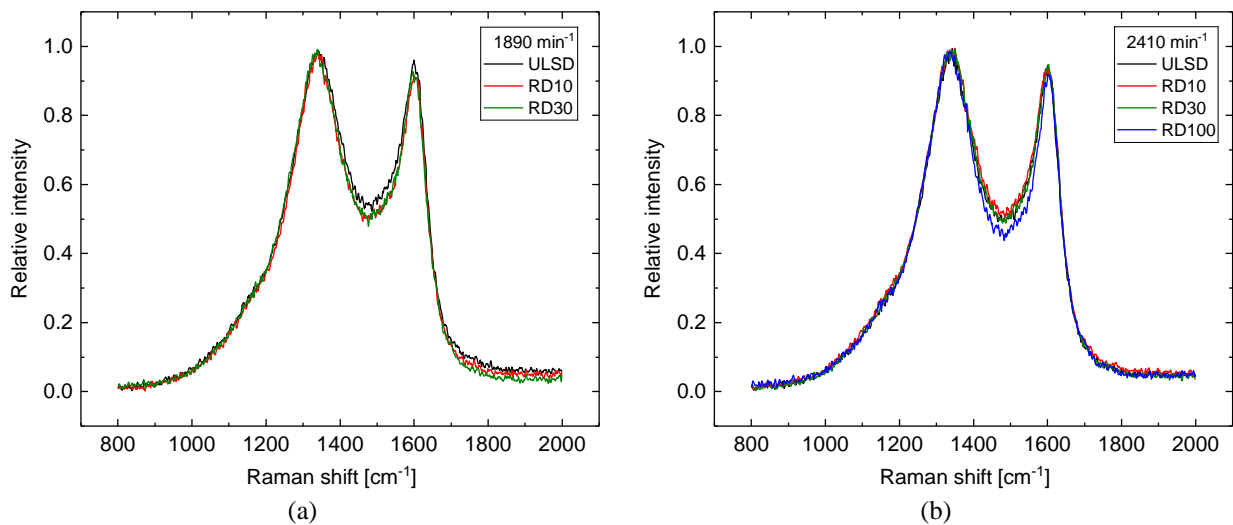
Figure E1. Raman spectra of samples taken at 1890 min^{-1} (a) and 2410 min^{-1} (b).
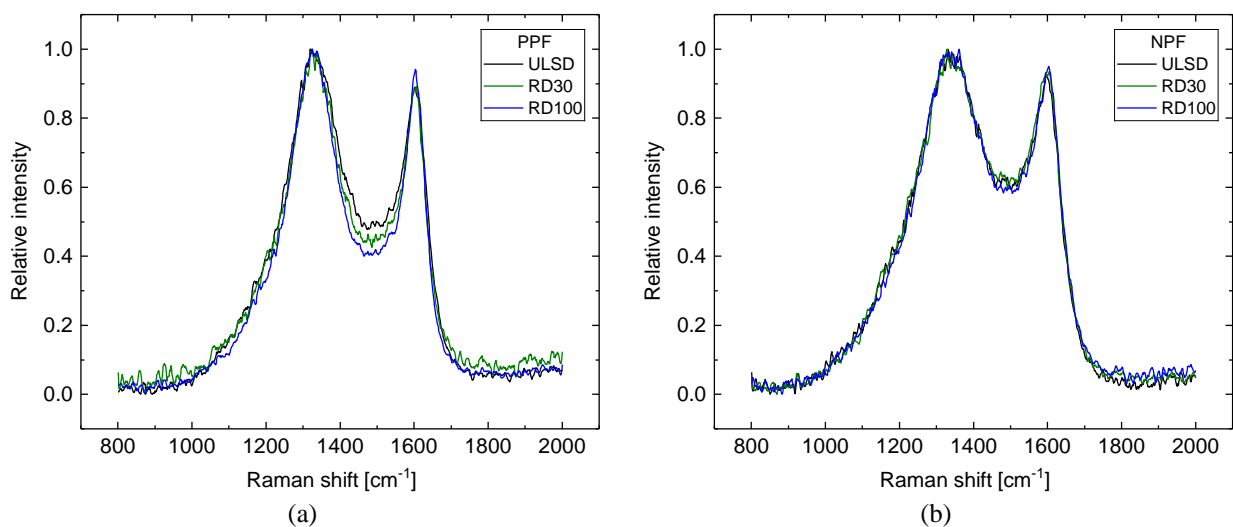
Figure E2. Raman spectra of samples generated in partially premixed flames (a) and non-premixed flames (b).

Table E1. Areas of the deconvoluted bands and their ratios to G band.

Diesel engine

Speed	Fuel	Band	Area	Area (±)	A_D/A_G	A_D/A_G (±)
1890	ULSD	D4	13.07	1.34	0.24	0.03
		D1	236.34	2.49	4.36	0.10
		D3	38.82	0.89	0.72	0.02
		G	54.25	1.20	-	-
	RD10	D4	16.54	1.01	0.30	0.02
		D1	230.12	7.69	4.24	0.05
		D3	37.46	1.72	0.69	0.02
		G	54.33	1.65	-	-
	RD30	D4	16.07	3.14	0.27	0.06
		D1	248.96	5.83	4.25	0.03
		D3	33.49	1.76	0.57	0.04
		G	58.55	1.66	-	-
2410	ULSD	D4	15.84	2.27	0.28	0.04
		D1	232.30	5.04	4.12	0.07
		D3	36.37	0.33	0.65	0.03
		G	56.43	2.22	-	-
	RD10	D4	14.88	1.05	0.26	0.02
		D1	234.28	3.77	4.15	0.09
		D3	36.27	0.94	0.64	0.01
		G	56.52	0.66	-	-
	RD30	D4	15.34	1.23	0.26	0.02
		D1	237.49	5.06	4.03	0.17
		D3	35.09	1.29	0.60	0.03
		G	58.99	1.64	-	-
	RD	D4	20.07	2.48	0.33	0.05
		D1	230.02	12.00	3.71	0.10
		D3	27.25	1.74	0.44	0.02
		G	61.89	1.82	-	-

Flame burners

Burner	Fuel	Band	Area	Area (±)	AD/AG	AD/AG (±)
NPF	ULSD	D4	17.43	4.32	0.35	0.11
		D1	303.67	14.69	6.04	0.52
		D3	40.59	0.32	0.81	0.11
		G	50.64	6.11	-	-
	RD30	D4	14.74	1.93	0.28	0.06
		D1	310.39	21.47	5.82	0.04
		D3	39.90	0.28	0.75	0.06
		G	53.37	3.75	-	-
	RD	D4	13.18	1.48	0.25	0.03
		D1	280.99	4.00	5.34	0.20
		D3	35.38	1.44	0.67	0.05
		G	52.72	2.73	-	-
PPF	ULSD	D4	7.07	1.67	0.15	0.03
		D1	239.33	5.30	5.05	0.28
		D3	33.70	2.67	0.71	0.10
		G	47.49	3.59	-	-
	RD30	D4	6.47	2.62	0.15	0.08
		D1	213.86	12.47	4.87	0.50
		D3	27.10	2.72	0.62	0.11
		G	44.23	5.58	-	-
	RD	D4	8.31	1.12	0.17	0.02
		D1	213.13	7.37	4.29	0.40
		D3	27.04	2.86	0.55	0.09
		G	49.91	3.33	-	-

Appendix F
Related to X-Ray diffraction analysis
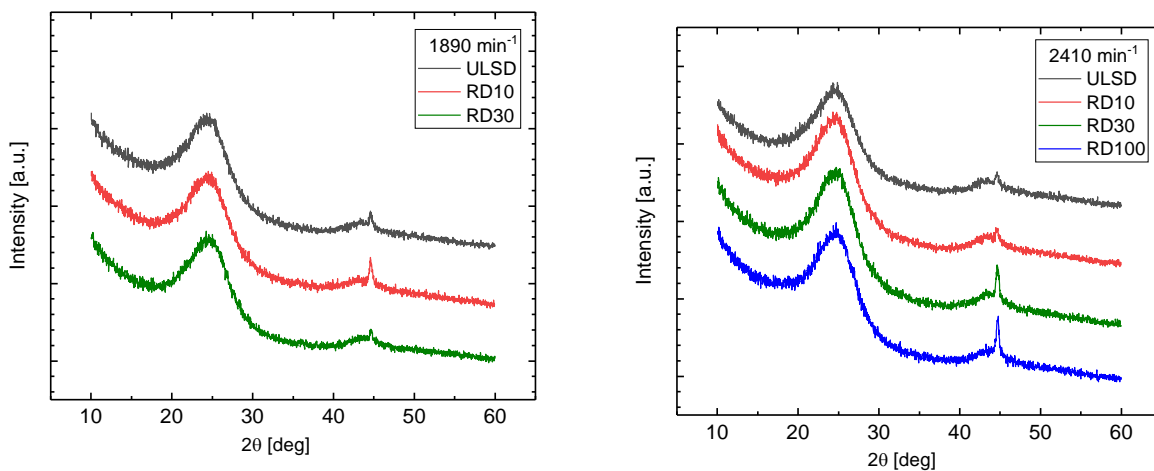
Figure F1. XRD spectra of samples taken at 1890 min^{-1}(a) and 2410 min^{-1} (b).
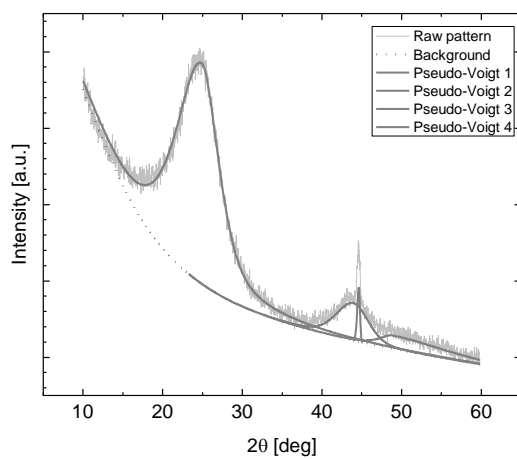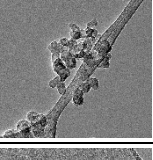

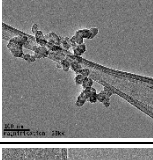Figure F2. XRD spectra and curve fit.
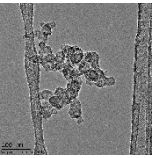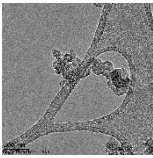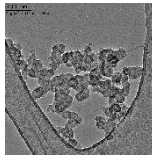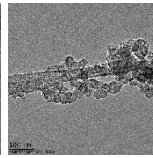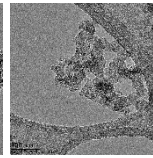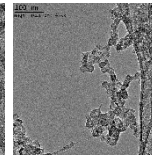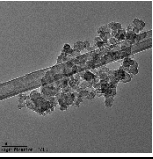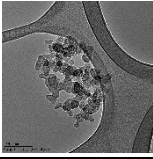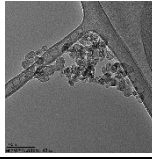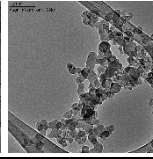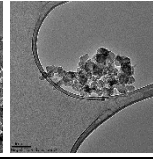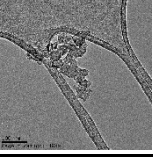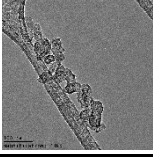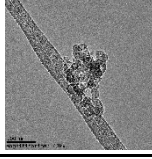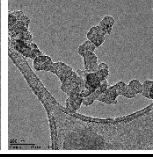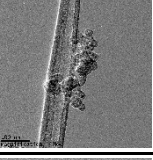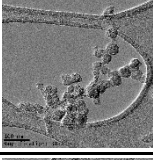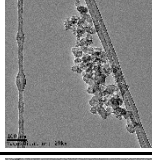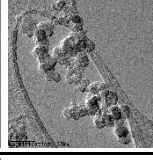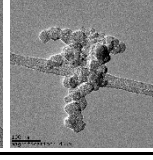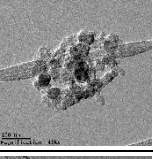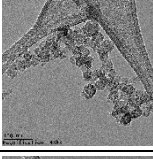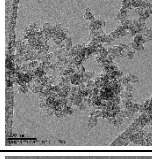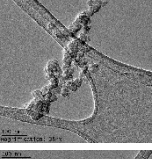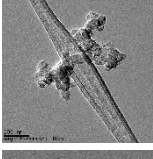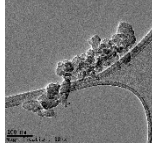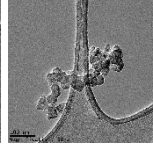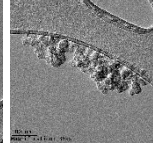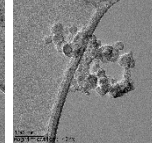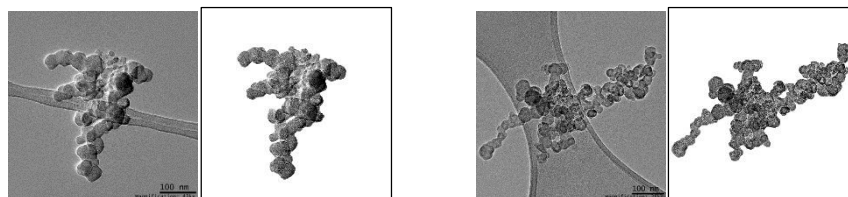
Table F1. XRD deconvolution results.

Speed	Fuel	2-Theta	Height	Area	Shape	FWHM	Res. Error (%)
1890	ULSD	24.61	1183	373587	0.555v	6.660	2.80
		44.47	127	1727	0.000v	0.339	
		43.84	203	41314	0.680v	4.043	
		48.04	65	23876	0.000v	9.813	
	RD10	24.69	1141	360594	0.558v	6.668	2.62
		44.50	280	5213	0.434v	0.397	
		43.41	170	40773	0.309v	5.449	
		49.40	64	26087	0.000v	12.126	
	RD30	24.78	1143	359310	0.575v	6.601	2.70
		44.56	112	1346	0.000v	0.300	
		43.91	191	46009	0.508v	5.112	
		49.90	71	27340	0.000v	11.216	
2410	ULSD	24.73	1408	437103	0.531v	6.591	2.85
		44.51	103	1527	0.000v	0.370	
		43.93	215	35032	0.000v	4.040	
		47.37	90	34850	0.387v	9.972	
	RD10	24.77	1071	333184	0.483v	6.700	2.95
		44.51	112	2057	0.000v	0.458	
		43.27	205	53074	0.769v	5.115	
		51.08	59	23317	0.065v	10.316	
	RD30	24.89	1445	451307	0.631v	6.460	2.54
		44.63	356	5980	0.000v	0.415	
		48.94	88	34147	0.695v	10.163	
		43.96	246	51481	0.265v	4.771	
	RD	25.03	1302	413006	0.606v	6.658	2.93
		44.63	406	6098	0.040v	0.368	
		44.23	249	51397	0.394v	4.485	
		47.94	101	41414	0.000v	11.376	

Appendix G
Related to transmission electron microscopy

Table G1. TEM images used for estimation of mean primary particle diameter.

Speed	Fuel	Magnification: 29.000x – 43.000x
1890	ULSD	
	RD10	
	RD30	
2410	ULSD	
	RD10	
	RD30	
	RD	

ULSD   RD

Figure G1. Example of images used for calculate the fractal dimension
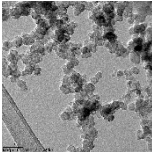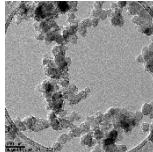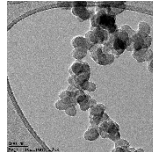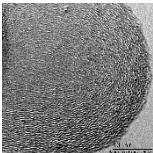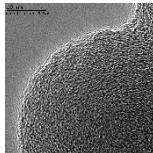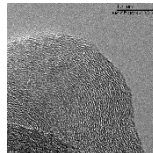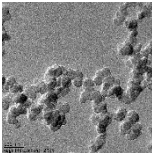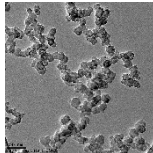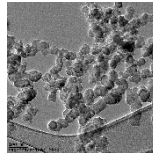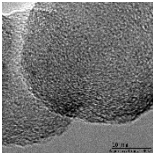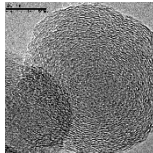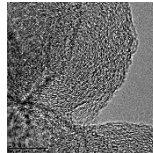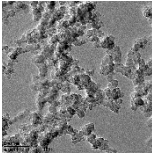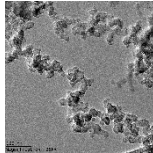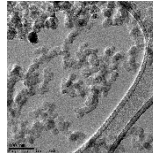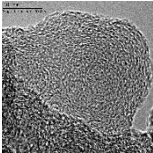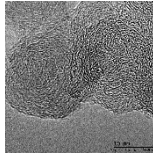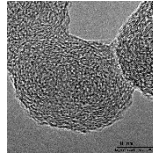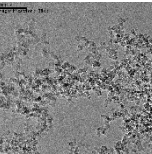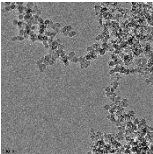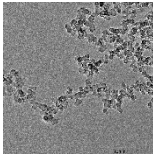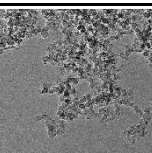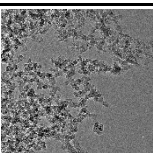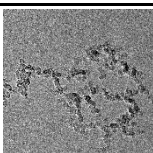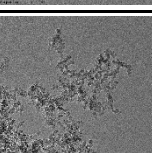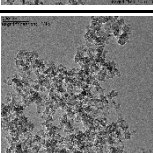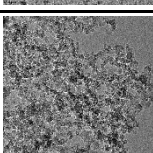
Table G2. Image processing parameters used in fringe analysis.

Magnification	Spatial resolution [nm/pixel]	Gaussian filter size [pixel]	Disk size for black top-hat operation [pixel]
450.000x	0.024	2	5
590.000x	0.019	3	6

Table G3. HRTEM images of diesel engine samples used for fringe analysis.

Speed	Fuel	Magnification: 450.000x
1890	ULSD	
	RD10	
	RD30	
2410	ULSD	
	RD10	
	RD30	
	RD	

Table G4. TEM and HRTEM images of the samples from flame burners.

Burner	Fuel	Magnification: 29.000x – 43.000x	Magnification: 590.000x
NPF	ULSD		
	RD30		
	RD		
PPF	ULSD		
	RD30		
	RD		

Figure G1. Example of blurred HRTEM images of PPF sample due to high instability of the particle.

REFERENCES

[1] BP. *BP Energy Outlook: 2018 edition*. BP p.l.c., 2018, London, UK.

[2] Benbrahim-Tallaa L., Baan R.A., Grosse Y., Lauby-Secretan B., El Ghissassi F., Bouvard V., et al. *Carcinogenicity of diesel-engine and gasoline-engine exhausts and some nitroarenes*. The Lancet Oncology 13 (2012) 663-664.

[3] Schröder O., Bünger J., Munack A., Knothe G., Krahl J. *Exhaust emissions and mutagenic effects of diesel fuel, biodiesel and biodiesel blends*. Fuel 103 (2013) 414-420.

[4] Agarwal A.K. *Biofuels (alcohols and biodiesel) applications as fuels for internal combustion engines*. Progress in Energy and Combustion Science 33 (2007) 233-271.

[5] Hartikka T., Kuronen M., Kiiski U. *Technical Performance of HVO (Hydrotreated Vegetable Oil) in Diesel Engines*. SAE Technical Paper 2012-01-1585 (2012)

[6] Sun C., Kang D., Bohac S.V., Boehman A.L. *Impact of Fuel and Injection Timing on Partially Premixed Charge Compression Ignition Combustion*. Energy & Fuels 30 (2016) 4331-4345.

[7] Lapuerta M., Villajos M., Agudelo J.R., Boehman A.L. *Key properties and blending strategies of hydrotreated vegetable oil as biofuel for diesel engines*. Fuel Processing Technology 92 (2011) 2406-2411.

[8] Aatola H., Larmi M., Sarjovaara T., Mikkonen S. *Hydrotreated Vegetable Oil (HVO) as a Renewable Diesel Fuel: Trade-off between NOx, Particulate Emission, and Fuel Consumption of a Heavy Duty Engine*. SAE Int. J. Engines 2008-01-2500 (2008) 1251-1262.

[9] Bezergianni S., Dimitriadis A. *Comparison between different types of renewable diesel*. Renewable and Sustainable Energy Reviews 21 (2013) 110-116.

[10] No S.-Y. *Application of hydrotreated vegetable oil from triglyceride based biomass to CI engines – A review*. Fuel 115 (2014) 88-96.

[11] Gill S.S., Tsolakis A., Dearn K.D., Rodríguez-Fernández J. *Combustion characteristics and emissions of Fischer–Tropsch diesel fuels in IC engines*. Progress in Energy and Combustion Science 37 (2011) 503-523.

[12] Huber G.W., O'Connor P., Corma A. *Processing biomass in conventional oil refineries: Production of high quality diesel by hydrotreating vegetable oils in heavy vacuum oil mixtures*. Applied Catalysis A: General 329 (2007) 120-129.

[13] Liu Y., Sotelo-Boyás R., Murata K., Minowa T., Sakanishi K. *Hydrotreatment of Vegetable Oils to Produce Bio-Hydrogenated Diesel and Liquefied Petroleum Gas Fuel over Catalysts Containing Sulfided Ni–Mo and Solid Acids*. Energy & Fuels 25 (2011) 4675-4685.

[14] Stumborg M., Wong A., Hogan E. *Hydroprocessed vegetable oils for diesel fuel improvement*. Bioresource Technology 56 (1996) 13-18.

[15] Jaroonjitsathian S., Saisirirat P., Sivara K., Tongroon M., Chollacoop N. *Effects of GTL and HVO Blended Fuels on Combustion and Exhaust Emissions of a Common-Rail DI Diesel Technology*. SAE Technical Paper 2014-01-2763 (2014)

[16] Gowdagiri S., Cesari X.M., Huang M., Oehlschlaeger M.A. *A diesel engine study of conventional and alternative diesel and jet fuels: Ignition and emissions characteristics*. Fuel 136 (2014) 253-260.

[17] Mattson J.M.S., Depcik C. *First and Second Law Heat Release Analysis in a Single Cylinder Engine*. SAE Int. J. Engines 9 (2016) 536-545.

[18] Hemanandh J., Narayanan K.V. *Production of Green Diesel by Hydrotreatment Using Jatropha Oil: Performance and Emission Analysis*. Waste and Biomass Valorization 8 (2017) 1931-1939.

[19] Pflaum H., Hofmann P., Geringer B., Weissel W. *Potential of Hydrogenated Vegetable Oil (HVO) in a Modern Diesel Engine*. SAE Technical Paper 2010-32-0081 (2010)

[20] Erkkilä K., Nylund N.-O., Hulkkonen T., Tilli A., Mikkonen S., Saikkonen P., et al. *Emission performance of paraffinic HVO diesel fuel in heavy duty vehicles*. SAE Technical Paper 2011-01-1966 (2011)

[21] Mizushima N., Sato S., Kawano D., Saito A., Takada Y. *A Study on NOx Emission Characteristics When Using Biomass-derived Diesel Alternative Fuels*. SAE Int. J. Fuels Lubr. 5 (2012) 892-899.

[22] Bhardwaj O.P., Kolbeck A.F., Kkoerfer T., Honkanen M. *Potential of Hydrogenated Vegetable Oil (HVO) in Future High Efficiency Combustion System*. SAE Int. J. Fuels Lubr. 6 (2013) 157-169.

[23] Kim D., Kim S., Oh S., No S.-Y. *Engine performance and emission characteristics of hydrotreated vegetable oil in light duty diesel engines*. Fuel 125 (2014) 36-43.

[24] Hemanandh J., Narayanan K.V. *Emission and Performance analysis of hydrotreated refined sunflower oil as alternate fuel*. Alexandria Engineering Journal 54 (2015) 389-393.

[25] Ogunkoya D., Roberts W.L., Fang T., Thapaliya N. *Investigation of the effects of renewable diesel fuels on engine performance, combustion, and emissions*. Fuel 140 (2015) 541-554.

[26] Rantanen L., Linnaila R., Aakko P., Harju T. *NExBTL - Biodiesel Fuel of the Second Generation*. SAE Technical Paper 2005-01-3771 (2005)

[27] Kuronen M., Mikkonen S., Aakko P., Murtonen T. *Hydrotreated Vegetable Oil as Fuel for Heavy Duty Diesel Engines*. SAE Technical Paper 2007-01-4031 (2007)

[28] Murtonen T., Aakko-Saksa P., Kuronen M., Mikkonen S., Lehtoranta K. *Emissions with Heavy-duty Diesel Engines and Vehicles using FAME, HVO and GTL Fuels with and without DOC+POC Aftertreatment*. SAE Int. J. Fuels Lubr. 2 (2009) 147-166.

[29] Westphal G.A., Krahl J., Munack A., Rosenkranz N., Schröder O., Schaak J., et al. *Combustion of Hydrotreated Vegetable Oil and Jatropha Methyl Ester in a Heavy Duty Engine: Emissions and Bacterial Mutagenicity*. Environmental Science & Technology 47 (2013) 6038-6046.

[30] Götz K., Singer A., Schröder O., Pabst C., Munack A., Bünger J., et al. *Exhaust Gas Emissions from Heavy-Duty Engines and Passenger Cars with Different After-Treatment Systems Running on Hydrotreated Vegetable Oil (HVO)*. SAE Technical Paper 2014-01-2827 (2014)

[31] Imperato M., Tilli A., Sarjovaara T., Larmi M. *Large-Bore Compression-Ignition Engines: High NOx Reduction Achieved at Low Load with Hydro-Treated Vegetable Oil*. SAE Int. J. Fuels Lubr. 5 (2011) 225-232.

[32] Lehto K., Elonheimo A., Hakkinen K., Sarjovaara T., Larmi M. *Emission Reduction Using Hydrotreated Vegetable Oil (HVO) With Miller Timing and EGR in Diesel Combustion*. SAE Int. J. Fuels Lubr. 5 (2011) 218-224.

[33] Sugiyama K., Goto I., Kitano K., Mogi K., Honkanen M. *Effects of Hydrotreated Vegetable Oil (HVO) as Renewable Diesel Fuel on Combustion and Exhaust Emissions in Diesel Engine*. SAE Int. J. Fuels Lubr. 5 (2011) 205-217.

[34] Happonen M., Heikkilä J., Murtonen T., Lehto K., Sarjovaara T., Larmi M., et al. *Reductions in Particulate and NOx Emissions by Diesel Engine Parameter Adjustments with HVO Fuel*. Environmental Science & Technology 46 (2012) 6198-6204.

[35] Heikkilä J., Happonen M., Murtonen T., Lehto K., Sarjovaara T., Larmi M., et al. *Study of Miller timing on exhaust emissions of a hydrotreated vegetable oil (HVO)-fueled diesel engine*. Journal of the Air & Waste Management Association 62 (2012) 1305-1312.

[36] Imperato M., Sarjovaara T., Larmi M., Tilli A. *Hydrotreated Vegetable Oil and Miller Timing in a Medium-Speed CI Engine*. SAE Technical Paper 2012-01-0862 (2012)

[37] Murtonen T., Aakko-Saksa P., Koponen P., Lehto K., Sarjovaara T., Happonen M., et al. *Emission Reduction Potential with Paraffinic Renewable Diesel by Optimizing Engine Settings or Using Oxygenate*. SAE Technical Paper 2012-01-1590 (2012)

[38] Bohl T., Smallbone A., Tian G., Roskilly A.P. *Particulate number and NOx trade-off comparisons between HVO and mineral diesel in HD applications*. Fuel 215 (2018) 90-101.

[39] Singh D., Subramanian K.A., Garg M.O. *Comprehensive review of combustion, performance and emissions characteristics of a compression ignition engine fueled with hydroprocessed renewable diesel*. Renewable and Sustainable Energy Reviews 81 (2018) 2947-2954.

[40] Happonen M., Lähde T., Messing M.E., Sarjovaara T., Larmi M., Wallenberg L.R., et al. *The comparison of particle oxidation and surface structure of diesel soot particles between fossil fuel and novel renewable diesel fuel*. Fuel 89 (2010) 4008-4013.

[41] Bhardwaj O., Lüers B., Holderbaum B., Körfer T., Pischinger S., Honkanen M. *Utilization of HVO Fuel Properties in a High Efficiency Combustion System: Part 2: Relationship of Soot Characteristics with its Oxidation Behavior in DPF*. SAE Int. J. Fuels Lubr. 2014-01-2846 (2014)

[42] Bhardwaj O., Lüers B., Holderbaum B., Körfer T., Pischinger S., Honkanen M. *Utilization of HVO Fuel Properties in a High Efficiency Combustion System: Impact of Soot Structure on the Diesel*

Particulate Filter Regeneration Behavior. International Journal of Automotive Engineering 6 (2015) 75-82.

[43] Lapuerta M., Rodríguez-Fernández J., Sánchez-Valdepeñas J., Salgado M.S. *Multi-Technique Analysis of Soot Reactivity from Conventional and Paraffinic Diesel Fuels*. Flow Turbulence Combust 96 (2016) 327-341.

[44] Rodríguez-Fernández J., Hernández J.J., Sánchez-Valdepeñas J. *Effect of oxygenated and paraffinic alternative diesel fuels on soot reactivity and implications on DPF regeneration*. Fuel 185 (2016) 460-467.

[45] Rodríguez-Fernández J., Lapuerta M., Sánchez-Valdepeñas J. *Regeneration of diesel particulate filters: Effect of renewable fuels*. Renewable Energy 104 (2017) 30-39.

[46] Sun C. *Nanostructure and Reactivity of Soot Produced from Partially Premixed Charge Compression Ignition (PCCI) Combustion and Post Injection*. University of Michigan PhD Thesis (2017)

[47] Song J., Alam M., Boehman A.L. *Impact of alternative fuels on soot properties and DPF regeneration*. Combustion Science and Technology 179 (2007) 1991-2037.

[48] Song J., Alam M., Boehman A.L., Kim U. *Examination of the oxidation behavior of biodiesel soot*. Combustion and Flame 146 (2006) 589-604.

[49] Yehliu K., Vander Wal R.L., Armas O., Boehman A.L. *Impact of fuel formulation on the nanostructure and reactivity of diesel soot*. Combustion and Flame 159 (2012) 3597-3606.

[50] Daly H.M., Horn A.B. *Heterogeneous chemistry of toluene, kerosene and diesel soots*. Physical Chemistry Chemical Physics 11 (2009) 1069-1076.

[51] Merchan-Merchan W., Sanmiguel S.G., McCollam S. *Analysis of soot particles derived from biodiesels and diesel fuel air-flames*. Fuel 102 (2012) 525-535.

[52] Merchan-Merchan W., Abdihamzehkolaei A., Merchan-Breuer D.A. *Formation and evolution of carbon particles in coflow diffusion air flames of vaporized biodiesel, diesel and biodiesel-diesel blends*. Fuel 226 (2018) 263-277.

[53] Witkowski D., Kondo K., Vishwanathan G., Rothamer D. *Evaluation of the sooting properties of real fuels and their commonly used surrogates in a laminar co-flow diffusion flame*. Combustion and Flame 160 (2013) 1129-1141.

[54] Barrientos E.J., Maricq M.M., Boehman A.L., Anderson J.E. *Impact of Ester Structures on the Soot Characteristics and Soot Oxidative Reactivity of Biodiesel*. SAE Technical Paper 2015-01-1080 (2015)

[55] Pérez W., Marín J., del Río J., Peña J., Rios L. *Upgrading of palm oil renewable diesel through hydroisomerization and formulation of an optimal blend*. Fuel 209 (2017) 442-448.

[56] Benjumea P., Agudelo J.R., Agudelo A.F. *Effect of the Degree of Unsaturation of Biodiesel Fuels on Engine Performance, Combustion Characteristics, and Emissions*. Energy & Fuels 25 (2011) 77-85.

[57] Huang C.-H., Vander Wal R.L. *Partial premixing effects upon soot nanostructure*. Combustion and Flame 168 (2016) 403-408.

[58] Dec J.E. *A Conceptual Model of DI Diesel Combustion Based on Laser-Sheet Imaging**. (1997)

[59] Love N.D., Parthasarathy R.N., Gollahalli S.R. *Rapid Characterization of Radiation and Pollutant Emissions of Biodiesel and Hydrocarbon Liquid Fuels*. Journal of Energy Resources Technology 131 (2009) 012202-012202-9.

[60] Singh V., Parthasarathy R.N., Gollahalli S.R. *Radiative Heat Transfer and Fluorescence Measurements in Laminar Prevaporized Canola Methyl Ester/Diesel Blend Flames*. Journal of Thermal Science and Engineering Applications 8 (2015) 011006-011006-10.

[61] Ruiz F.A., Cadrazco M., López A.F., Sanchez-Valdepeñas J., Agudelo J.R. *Impact of dual-fuel combustion with n-butanol or hydrous ethanol on the oxidation reactivity and nanostructure of diesel particulate matter*. Fuel 161 (2015) 18-25.

[62] Soriano J.A., Agudelo J.R., López A.F., Armas O. *Oxidation reactivity and nanostructural characterization of the soot coming from farnesane - A novel diesel fuel derived from sugar cane*. Carbon 125 (2017) 516-529.

[63] Rodríguez-Fernández J., Oliva F., Vázquez R.A. *Characterization of the Diesel Soot Oxidation Process through an Optimized Thermogravimetric Method*. Energy & Fuels 25 (2011) 2039-2048.

[64] Al-Qurashi K., Boehman A.L. *Impact of exhaust gas recirculation (EGR) on the oxidative reactivity of diesel engine soot*. Combustion and Flame 155 (2008) 675-695.

[65] Lapuerta M., Oliva F., Agudelo J.R., Stitt J.P. *Optimization of Raman Spectroscopy Parameters for Characterizing Soot from Different Diesel Fuels*. Combustion Science and Technology 183 (2011) 1203-1220.

[66] Lapuerta M., Oliva F., Agudelo J.R., Boehman A.L. *Effect of fuel on the soot nanostructure and consequences on loading and regeneration of diesel particulate filters*. Combustion and Flame 159 (2012) 844-853.

[67] Lapuerta M., Ballesteros R., Martos F.J. *A method to determine the fractal dimension of diesel soot agglomerates*. Journal of Colloid and Interface Science 303 (2006) 149-158.

[68] Lapuerta M., Martos F.J., Martín-González G. *Geometrical determination of the lacunarity of agglomerates with integer fractal dimension*. Journal of Colloid and Interface Science 346 (2010) 23-31.

[69] Botero M.L., Chen D., González-Calera S., Jefferson D., Kraft M. *HRTEM evaluation of soot particles produced by the non-premixed combustion of liquid fuels*. Carbon 96 (2016) 459-473.

[70] Santamaría A., Mondragón F., Molina A., Marsh N.D., Eddings E.G., Sarofim A.F. *FT-IR and 1H NMR characterization of the products of an ethylene inverse diffusion flame*. Combustion and Flame 146 (2006) 52-62.

[71] Smith M., Scudiero L., Espinal J., McEwen J.-S., Garcia-Perez M. *Improving the deconvolution and interpretation of XPS spectra from chars by ab initio calculations*. Carbon 110 (2016) 155-171.

[72] Gómez A., Armas O., Lilik G.K., Boehman A. *Estimation of volatile organic emission based on diesel particle size distributions*. Measurement Science and Technology 23 (2012) 105305.

[73] Jansma H., Fino D., Uitz R., Makkee M. *Influence of Diesel Fuel Characteristics on Soot Oxidation Properties*. Industrial & Engineering Chemistry Research 51 (2012) 7559-7564.

[74] Wei J., Song C., Lv G., Song J., Wang L., Pang H. *A comparative study of the physical properties of in-cylinder soot generated from the combustion of n-heptane and toluene/n-heptane in a diesel engine*. Proceedings of the Combustion Institute 35 (2015) 1939-1946.

[75] Hurt R.H., Crawford G.P., Shim H.-S. *Equilibrium nanostructure of primary soot particles*. Proceedings of the Combustion Institute 28 (2000) 2539-2546.

[76] Yehliu K., Armas O., Vander Wal R.L., Boehman A.L. *Impact of engine operating modes and combustion phasing on the reactivity of diesel soot*. Combustion and Flame 160 (2013) 682-691.

[77] Vander Wal R.L., Tomasek A.J. *Soot oxidation: dependence upon initial nanostructure*. Combustion and Flame 134 (2003) 1-9.

[78] Wang L., Song C., Song J., Lv G., Pang H., Zhang W. *Aliphatic C–H and oxygenated surface functional groups of diesel in-cylinder soot: Characterizations and impact on soot oxidation behavior*. Proceedings of the Combustion Institute 34 (2013) 3099-3106.

[79] Agudelo J.R., Álvarez A., Armas O. *Impact of crude vegetable oils on the oxidation reactivity and nanostructure of diesel particulate matter*. Combustion and Flame 161 (2014) 2904-2915.

[80] Neeft J.P.A., Nijhuis T.X., Smakman E., Makkee M., Moulijn J.A. *Kinetics of the oxidation of diesel soot*. Fuel 76 (1997) 1129-1136.

[81] Seong H.J., Boehman A.L. *Studies of soot oxidative reactivity using a diffusion flame burner*. Combustion and Flame 159 (2012) 1864-1875.

[82] Kittelson D.B. *Engines and nanoparticles: a review*. Journal of Aerosol Science 29 (1998) 575-588.

[83] Yamane K., Asakawa T., Numao H., Komori M. *Characteristics of DPF for Diesel Engine Fueled With Biodiesel Fuel - First Report: Self-Regeneration Behavior on Vehicle Road Test and Engine Bench Rig Test*. (2004)

[84] Jung H., Kittelson D.B., Zachariah M.R. *Characteristics of SME Biodiesel-Fueled Diesel Particle Emissions and the Kinetics of Oxidation*. Environmental Science & Technology 40 (2006) 4949-4955.

[85] Sadezky A., Muckenhuber H., Grothe H., Niessner R., Pöschl U. *Raman microspectroscopy of soot and related carbonaceous materials: Spectral analysis and structural information*. Carbon 43 (2005) 1731-1742.

[86] Marsh H. *A tribute to Philip L. Walker*. Carbon 29 (1991) 703-704.

[87] Singh D., Subramanian K.A., Singal S.K. *Emissions and fuel consumption characteristics of a heavy duty diesel engine fueled with Hydroprocessed Renewable Diesel and Biodiesel*. Applied Energy 155 (2015) 440-446.

[88] Ban-Weiss G.A., Chen J.Y., Buchholz B.A., Dibble R.W. *A numerical investigation into the anomalous slight NOx increase when burning biodiesel; A new (old) theory*. Fuel Processing Technology 88 (2007) 659-667.

[89] Boehman A.L., Song J., Alam M. *Impact of Biodiesel Blending on Diesel Soot and the Regeneration of Particulate Filters*. Energy & Fuels 19 (2005) 1857-1864.

[90] Vander Wal R.L., Yezerets A., Currier N.W., Kim D.H., Wang C.M. *HRTEM Study of diesel soot collected from diesel particulate filters*. Carbon 45 (2007) 70-77.

[91] Vander Wal R.L., Bryg V.M., Hays M.D. *Fingerprinting soot (towards source identification): Physical structure and chemical composition*. Journal of Aerosol Science 41 (2010) 108-117.

[92] Song J., Lee K.O. *Fuel Property Impacts on Diesel Particulate Morphology, Nanostructures, and NOx Emissions*. SAE Technical Paper 2007-01-0129 (2007)

[93] Lee K.O., Cole R., Sekar R., Choi M.Y., Kang J.S., Bae C.S., et al. *Morphological investigation of the microstructure, dimensions, and fractal geometry of diesel particulates*. Proceedings of the Combustion Institute 29 (2002) 647-653.

[94] Neer A., Koylu U.O. *Effect of operating conditions on the size, morphology, and concentration of submicrometer particulates emitted from a diesel engine*. Combustion and Flame 146 (2006) 142-154.

[95] Chandler M.F., Teng Y., Koylu U.O. *Diesel engine particulate emissions: A comparison of mobility and microscopy size measurements*. Proceedings of the Combustion Institute 31 (2007) 2971-2979.

[96] Lapuerta M., Martos F.J., Herreros J.M. *Effect of engine operating conditions on the size of primary particles composing diesel soot agglomerates*. Journal of Aerosol Science 38 (2007) 455-466.

[97] Lu T., Cheung C.S., Huang Z. *Effects of engine operating conditions on the size and nanostructure of diesel particles*. Journal of Aerosol Science 47 (2012) 27-38.

[98] Gupta S., Cole R., Vazquez F.M., Sekar R. *Particulate Emissions From a Modern Light Duty CIDI Engine*. (2002)

[99] Vander Wal R.L., Mueller C.J. *Initial Investigation of Effects of Fuel Oxygenation on Nanostructure of Soot from a Direct-Injection Diesel Engine*. Energy & Fuels 20 (2006) 2364-2369.

[100] Zhang H.R., Eddings E.G., Sarofim A.F. *Criteria for selection of components for surrogates of natural gas and transportation fuels*. Proceedings of the Combustion Institute 31 (2007) 401-409.

[101] Zhang H.R., Eddings E.G., Sarofim A.F. *COMBUSTION REACTIONS OF PARAFFIN COMPONENTS IN LIQUID TRANSPORTATION FUELS USING GENERIC RATES*. Combustion Science and Technology 179 (2007) 61-89.

[102] Ishiguro T., Suzuki N., Fujitani Y., Morimoto H. *Microstructural changes of diesel soot during oxidation*. Combustion and Flame 85 (1991) 1-6.

[103] Müller J.O., Su D.S., Wild U., Schlögl R. *Bulk and surface structural investigations of diesel engine soot and carbon black*. Physical Chemistry Chemical Physics 9 (2007) 4018-4025.

[104] Vander Wal R.L., Bryg V.M., Hays M.D. *XPS Analysis of Combustion Aerosols for Chemical Composition, Surface Chemistry, and Carbon Chemical State*. Analytical Chemistry 83 (2011) 1924-1930.

[105] Wu Y. *Flame Lift-Off and Blow-Out Stability Limits and Their Application in Gas Burners*. Handbook of Combustion (2010)

[106] Ladommatos N., Xiao Z., Zhao H. *Effects of fuels with a low aromatic content on diesel engine exhaust emissions*. Proceedings of the Institution of Mechanical Engineers, Part D: Journal of Automobile Engineering 214 (2000) 779-794.

[107] kent J.H., Wagner H.G. *Who do Diffusion flames Emit smoke*. Combustion Science and Technology 41 (1984) 245-269.

[108] Velásquez M., Mondragón F., Santamaría A. *Chemical characterization of soot precursors and soot particles produced in hexane and diesel surrogates using an inverse diffusion flame burner*. Fuel 104 (2013) 681-690.

[109] Botero M.L., Mosbach S., Kraft M. *Sooting tendency and particle size distributions of n-heptane/toluene mixtures burned in a wick-fed diffusion flame*. Fuel 169 (2016) 111-119.

[110] Botero M.L., Mosbach S., Kraft M. *Sooting tendency of paraffin components of diesel and gasoline in diffusion flames*. Fuel 126 (2014) 8-15.

[111] Mauss F., Trilken B., Breitbach H., Peters N. *Soot Formation in Partially Premixed Diffusion Flames at Atmospheric Pressure*. Soot Formation in Combustion: Mechanisms and Models (1994) 325-349.

[112] Ng H., Biruduganti M., Stork K. *Comparing the Performance of SunDiesel™ and Conventional Diesel in a Light-Duty Vehicle and Heavy-Duty Engine*. (2005)

[113] Shukla P.C., Shamun S., Gren L., Malmborg V., Pagels J., Tuner M. *Investigation of Particle Number Emission Characteristics in a Heavy-Duty Compression Ignition Engine Fueled with Hydrotreated Vegetable Oil (HVO)*. (2018)

[114] Jones J.M., Jones D.H. *Modelling the competition between annealing and oxidation in the carbon–oxygen reaction*. Carbon 45 (2007) 677-680.

[115] Eastwood P. *Particulate Emissions from Vehicles*. John Wiley & Sons, 2008.

[116] Jaramillo I.C., Gaddam C.K., Vander Wal R.L., Huang C.-H., Levinthal J.D., Lighty J.S. *Soot oxidation kinetics under pressurized conditions*. Combustion and Flame 161 (2014) 2951-2965.

[117] Commodo M., Joo P.H., De Falco G., Minutolo P., D'Anna A., Gülder Ö.L. *Raman Spectroscopy of Soot Sampled in High-Pressure Diffusion Flames*. Energy & Fuels 31 (2017) 10158-10164.